Numer. Math. (2001) 88: 683–729
Digital Object Identifier (DOI) 10.1007/s002110000250

Numerische Mathematik

# A third-order semi-discrete genuinely multidimensional central scheme for hyperbolic conservation laws and related problems

**Alexander Kurganov, Guergana Petrova**

Department of Mathematics, University of Michigan, Ann Arbor, MI 48109-1109, USA; e-mail: {kurganov,petrova}@math.lsa.umich.edu

Received February 7, 2000 / Published online December 19, 2000 – 

**Summary.** We construct a new third-order semi-discrete genuinely multidimensional central scheme for systems of conservation laws and related convection-diffusion equations. This construction is based on a multidimensional extension of the idea, introduced in [17] – the use of more precise information about the *local speeds of propagation*, and integration over nonuniform control volumes, which contain Riemann fans.

As in the one-dimensional case, the small numerical dissipation, which is independent of $\mathcal{O}(\frac{1}{\Delta t})$, allows us to pass to a limit as $\Delta t \downarrow 0$. This results in a particularly simple genuinely multidimensional semi-discrete scheme. The high resolution of the proposed scheme is ensured by the new two-dimensional piecewise quadratic non-oscillatory reconstruction. First, we introduce a less dissipative modification of the reconstruction, proposed in [29]. Then, we generalize it for the computation of the two-dimensional numerical fluxes.

Our scheme enjoys the main advantage of the Godunov-type central schemes – *simplicity*, namely it does not employ Riemann solvers and characteristic decomposition. This makes it a universal method, which can be easily implemented to a wide variety of problems. In this paper, the developed scheme is applied to the Euler equations of gas dynamics, a convection-diffusion equation with strongly degenerate diffusion, the incompressible Euler and Navier-Stokes equations. These numerical experiments demonstrate the desired accuracy and high resolution of our scheme.

*Mathematics Subject Classification (1991):* 65M10, 65M05

*Correspondence to*: A. Kurganov

## 1 Introduction

We are interested in Godunov-type schemes for solving the multidimensional system of conservation laws

$$u_t + \nabla_{\mathbf{x}} \cdot f(u) = 0, \quad \mathbf{x} \in I\!R^d, \tag{1.1}$$

and the closely related convection-diffusion equations

$$u_t + \nabla_{\mathbf{x}} \cdot f(u) = \nabla_{\mathbf{x}} Q(u, \nabla_{\mathbf{x}} u), \quad \mathbf{x} \in I\!R^d, \tag{1.2}$$

subject to the initial data

$$u(\mathbf{x}, 0) = u_0(\mathbf{x}). \tag{1.3}$$

Here $Q$ satisfies the weak parabolicity condition $\nabla_{\mathbf{s}} Q(u, \mathbf{s}) \geq 0$ for all $(u, \mathbf{s})$.

Godunov-type schemes are projection-evolution methods, which at every time step consist of three consecutive stages – *reconstruction*, *evolution* and *projection*. First, a piecewise polynomial interpolant is reconstructed from the piecewise constant data (the cell-averages), computed at the previous time step. Then, the interpolant is evolved in time according to (1.1). Finally, the solution is projected onto a space of piecewise constants. Depending on the projection step, we distinguish two kinds of Godunov-type schemes – central and upwind.

The Godunov-type central schemes are based on exact evolution and averaging over Riemann fans. Therefore, in contrast to the Godunov-type upwind schemes, no characteristic decomposition or Riemann solvers are involved. This makes the central schemes simple, and they can be implemented as a 'black box solver' for the general multidimensional systems (1.1) and (1.2).

In the one-dimensional case, examples of such schemes are the first-order (staggered) Lax-Friedrichs scheme [19,7], the second-order Nessyahu-Tadmor scheme [31], and their higher-order generalizations [29,4,21]. Second-order multidimensional central schemes were introduced in [11, 2], and their higher-order extensions were developed in [22,23]. The advantage of the higher-order schemes is that they reduce the excessive numerical viscosity, typical for the Lax-Friedrichs scheme, and give much sharper resolution of the shocks and rarefactions.

We would also like to mention the central schemes for the Hamilton-Jacobi equations, recently developed in [25,26,18], the central schemes for incompressible flows in [12–14,16,24], and their applications to various systems, for example, [6,1,33].

Unfortunately, the aforementioned staggered central schemes may not provide a satisfactory resolution when small time steps are enforced by stability restrictions (e.g., this may occur when one applies these schemes to

the (degenerate) parabolic systems (1.2)). Another disadvantage of these schemes is that they cannot be used for steady-state computations, or equivalently, they do not admit semi-discrete form. The reason is in the accumulation of numerical dissipation, which is of order $\mathcal{O}(\frac{(\Delta x)^{2r}}{\Delta t})$, where $r$ is the formal order of the scheme.

These problems have been recently resolved in [17], where a new second-order Godunov-type central scheme is introduced. The proposed scheme has smaller dissipation ($\sim (\Delta t)^{2r-1}$), and thus it can be efficiently used with time steps as small as required. In the new construction, the evolution step is performed by integrating over non-equal control volumes, whose sizes are proportional to the *local speeds of propagation*. The evolved solution is then projected back onto the original grid in a more complicated manner, which requires an additional piecewise polynomial reconstruction. In this way, a *non-staggered* fully-discrete central scheme is derived. It can be naturally reduced to a particularly simple semi-discrete form (for details see [17]). The same idea was used in [16] to develop a third-order semi-discrete central scheme.

Both in [17] and [16], the multidimensional semi-discrete schemes were obtained by using a 'dimension-by-dimension' approach – the one-dimensional numerical flux was straightforwardly applied in all coordinate directions. In this paper, we present new high-order *genuinely multidimensional* semi-discrete central schemes. They are based on a multidimensional generalization of the one-dimensional construction, used in [17, 16], namely we first integrate over non-equal volumes to derive a fully-discrete scheme, and then we pass to a semi-discrete limit (we let $\Delta t \downarrow 0$, keeping $\Delta x$ fixed).

Semi-discrete central schemes consist of three independent building blocks – a piecewise polynomial reconstruction, a spatial flux discretization and an ODE solver. Our genuinely multidimensional recipe provides the numerical fluxes. For the other two blocks one can pick any *non-oscillatory* reconstruction and an efficient ODE solver.

For second-order schemes one uses a piecewise linear reconstruction – a library of such (essentially) non-oscillatory reconstructions is available (see e.g. [8,9,15,20,31,32]). To achieve a third-order accuracy, a piecewise quadratic approximation is needed. However, to build a *third-order non-oscillatory* interpolant is a highly nontrivial problem. In the one-dimensional case, one of the possibilities is to use the essentially non-oscillatory (ENO) reconstruction [9,35], or its weighted generalizations [28,10,21,23]. Multidimensional ENO-type reconstructions were introduced in [22,23]. A disadvantage of this approach is that it employs smoothness indicators, which require a certain a-priori information about the solution.

Alternative one-dimensional non-oscillatory piecewise quadratic reconstructions were proposed in [27,29]. They both satisfy the number of extrema

diminishing (NED) property and do not require the use of smoothness indicators. In this work, we present a less dissipative one-dimensional modification of the reconstruction from [29]. We also generalize the one-dimensional reconstruction for the computation of the two-dimensional numerical fluxes in our scheme.

The paper is organized as follows. In Sect. 2, we briefly describe the recent development of Godunov-type central schemes. Next, in Sect. 3.1, we present the one-dimensional modification of the non-oscillatory piecewise quadratic reconstruction from [29]. In Sects. 3.2 and 3.3, we develop our new genuinely multidimensional central scheme, which employs the multidimensional third-order reconstruction, introduced in Sect. 3.4. The results from our numerical experiments are shown in Sect. 4. We apply our third-order scheme to a variety of one- and two-dimensional problems, including the compressible Euler equations of gas dynamics, a convection-diffusion equation with a nonlinear degenerate diffusion, the incompressible Euler and Navier-Stokes equations. These numerical examples demonstrate the expected third-order accuracy and the high resolution of our scheme.

## 2 Godunov-type central schemes – an overview

In this section, we discuss Godunov-type central schemes. In Sect. 2.1, we recall the construction of staggered central schemes. Then, in Sect. 2.2, we review the recently proposed [17,16] semi-discrete central schemes. Finally, in Sect. 2.3, we briefly describe the one-dimensional non-oscillatory piecewise parabolic reconstruction from [29].

For the sake of simplicity, we will consider only uniform grids. Throughout this paper, we will use the following notation. Let $x_j := j\Delta x$, $x_{j\pm\frac{1}{2}} := (j \pm 1/2)\Delta x$, $t^n := n\Delta t$, $u_j^n := u(x_j, t^n)$, where $\Delta x$ and $\Delta t$ are small spatial and time scales, respectively.

### *2.1 Central schemes for conservation laws*

We begin with the definition of the sliding average of $u(\cdot, t)$,

$$\bar{u}(x,t) := \frac{1}{\Delta x} \int\limits_{I(x)} u(\xi, t)\, d\xi, \quad I(x) = \{\xi : |\xi - x| < \frac{\Delta x}{2}\}. \tag{2.1}$$

We then integrate (1.1) over $I(x) \times [t, t + \Delta t]$, and arrive at the equivalent formulation of the system (1.1),

$$\bar{u}(x, t + \Delta t) = \bar{u}(x,t) - \frac{1}{\Delta x}$$

$$\times\left[\int_{\tau=t}^{t+\Delta t} f(u(x+\frac{\Delta x}{2},\tau))\,d\tau - \int_{\tau=t}^{t+\Delta t} f(u(x-\frac{\Delta x}{2},\tau))\,d\tau\right]. \tag{2.2}$$

This is the starting point for the construction of Godunov-type schemes, which consists of three steps – *reconstruction*,*evolution* and *projection*.

**Reconstruction.** At time level $t = t^n$ a piecewise polynomial function $\widetilde{u}(x,t^n)$,

$$\widetilde{u}(x,t^n) = p_j^n(x), \qquad x_{j-\frac{1}{2}} < x < x_{j+\frac{1}{2}}, \quad \forall j, \tag{2.3}$$

is reconstructed from the data $\bar{u}_j^n := \bar{u}(x_j,t^n)$, computed at the previous time step. Here, $\{p_j^n\}$ are algebraic polynomials, and therefore $\widetilde{u}(\cdot,t^n)$ may be discontinuous only at $x_{j\pm\frac{1}{2}}$. The reconstruction is required to satisfy two basic properties –

• *conservation* of the given cell averges :

$$\int_{x_{j-\frac{1}{2}}}^{x_{j+\frac{1}{2}}} \widetilde{u}(\xi,t^n)\,d\xi = \bar{u}_j^n, \quad \forall j;$$

• *accuracy* (for smooth $u(x,t)$):

$$\widetilde{u}(x,t^n) = u(x,t^n) + \mathcal{O}((\Delta x)^r),$$

where $r$ is the (formal) order of the scheme to be constructed.

**Evolution.** The piecewise polynomial $\widetilde{u}(\cdot,t^n)$ is evolved exactly according to the integral equation (2.2), and the solution at time $t = t^{n+1}$ is obtained in terms of its sliding averages.

**Projection.** An evaluation of these sliding averages at particular grid points provides the approximate cell averages of the solution at the next time level, $\{\bar{u}^{n+1}\}$.

Choosing $x = x_j$ in (2.2) results in an upwind Godunov-type scheme. In this case, the solution of the initial value problem (1.1),(1.3) with initial data $u_0(x) = \widetilde{u}(x,t^n)$, prescribed at $t = t^n$, may be non-smooth in the neighborhood of the points $\{x_{j+\frac{1}{2}}\}$. Therefore, the evaluation of the flux integrals in (2.2) requires the use of a computationally expensive (approximate) Riemann solver and chraracteristic decomposition.

An alternative staggered grid approach, namely the choice of $x = x_{j+\frac{1}{2}}$ in (2.2), was proposed by Nessyahu and Tadmor [31]. In this case, (2.2)

leads to the Godunov-type *central* scheme

$$\bar{u}^{n+1}_{j+\frac{1}{2}} = \frac{1}{\Delta x}\left[\int\limits_{x_j}^{x_{j+\frac{1}{2}}} p^n_j(x)\,dx + \int\limits_{x_{j+\frac{1}{2}}}^{x_{j+1}} p^n_{j+1}(x)\,dx\right] -$$

$$-\frac{\lambda}{\Delta t}\left[\int\limits_{t^n}^{t^{n+1}} f(u(x_{j+1},t))\,dt - \int\limits_{t^n}^{t^{n+1}} f(u(x_j,t))\,dt\right], \quad \lambda := \frac{\Delta t}{\Delta x}. \tag{2.4}$$

In contrast to the upwind schemes, the RHS of (2.4) can be easily evaluated. The spatial integrals can be computed exactly for a given reconstruction $\{p^n_j\}$. Also, due to the finite speed of propagation, the solution of (1.1),(1.3) with $u_0(x) = \widetilde{u}(x,t^n)$ is smooth in $(x_j-\varepsilon, x_j+\varepsilon)\times[t^n,t^{n+1})$, under an appropriate CFL restriction on $\Delta t$. Hence, the flux integrals in (2.4) can be approximated by a quadrature formula of order $\geq r$. Notice that the function values, needed in the quadrature, may be computed either by Taylor expansion, or by a Runge-Kutta method ([29,4]).

For example, if we use the second-order reconstruction

$$p^n_j(x) = \bar{u}^n_j + s^n_j(x-x_j),$$

and the midpoint quadrature rule

$$\int\limits_{t^n}^{t^{n+1}} f(u(x_j,t))\,dt = \Delta t f(u(x_j,t^{n+1/2})) + \mathcal{O}((\Delta t)^2),$$

we arrive at the Nessyahu-Tadmor (NT) staggered central scheme

$$\bar{u}^{n+1}_{j+\frac{1}{2}} = \frac{1}{2}(\bar{u}^n_j + \bar{u}^n_{j+1}) - \frac{1}{8}(s^n_j - s^n_{j+1}) - \lambda\left[f(u^{n+\frac{1}{2}}_{j+1}) - f(u^{n+\frac{1}{2}}_j)\right],$$

where $u^{n+\frac{1}{2}}_j$ are evaluated, for example, by the Taylor expansion

$$u^{n+\frac{1}{2}}_j = \bar{u}^n_j - \frac{\Delta t}{2}(f_x)^n_j.$$

To ensure the non-oscillatory nature of the NT scheme, one should apply a nonlinear limiter while computing the slopes $\{s^n_j\}$. In the original NT scheme [31] the so-called *minmod* limiter [20,8,32] is used, namely, the slopes are determined by

$$s^n_j = \operatorname{minmod}\left(\frac{\bar{u}^n_j - \bar{u}^n_{j-1}}{\Delta x}, \frac{\bar{u}^n_{j+1} - \bar{u}^n_j}{\Delta x}\right), \tag{2.5}$$

where

$$\operatorname{minmod}(a,b) := \frac{\operatorname{sgn}(a)+\operatorname{sgn}(b)}{2}\min(|a|,|b|).$$

### *2.2 Semi-discrete central schemes*

As mentioned in the Introduction, the staggered central schemes do not admit semi-discrete formulation. This makes them inappropriate for steady state computations or for solving the diffusion dominated convection-diffusion systems (1.2). The encountered difficulties were recently resolved by the non-staggered central schemes, proposed in [17]. Next, we give a brief overview of these schemes.

We begin with a piecewise polynomial reconstruction $\{p_j^n\}$, which may be discontinuous at the interface points $\{x_{j+\frac{1}{2}}\}$. This discontinuities propagate with different speeds, whose upper bounds are

$$a^n_{j+\frac{1}{2}} := \max_{\omega\in C(u^{n-}_{j+\frac{1}{2}},u^{n+}_{j+\frac{1}{2}})} \rho\Big(\frac{\partial f}{\partial u}(\omega)\Big).$$

Here, $C(u^{n-}_{j+\frac{1}{2}}, u^{n+}_{j+\frac{1}{2}})$ is the curve in the phase space that connects $u^{n-}_{j+\frac{1}{2}} := p^n_j(x_{j+\frac{1}{2}})$ and $u^{n+}_{j+\frac{1}{2}} := p^n_{j+1}(x_{j+\frac{1}{2}})$, and $\rho\left(\frac{\partial f}{\partial u}\right)$ is the spectral radius of the Jacobian $\frac{\partial f}{\partial u}$. For example, in the genuinely nonlinear or linearly degenerate case, we have

$$a^n_{j+\frac{1}{2}} = \max\left\{\rho\Big(\frac{\partial f}{\partial u}(u^{n-}_{j+\frac{1}{2}})\Big), \rho\Big(\frac{\partial f}{\partial u}(u^{n+}_{j+\frac{1}{2}})\Big)\right\}.$$

The main idea in the constrtuction of the schemes in [17] is based on utilizing these CFL related *local* speeds of propagation. We consider the domains

$$[x^n_{j-\frac{1}{2},r}, x^n_{j+\frac{1}{2},l}]\times[t^n,t^{n+1}] \quad \text{and} \quad [x^n_{j+\frac{1}{2},l}, x^n_{j+\frac{1}{2},r}]\times[t^n,t^{n+1}], \tag{2.6}$$

with $x^n_{j+\frac{1}{2},l} := x_{j+\frac{1}{2}} - \Delta t a^n_{j+\frac{1}{2}}$, and $x^n_{j+\frac{1}{2},r} := x_{j+\frac{1}{2}} + \Delta t a^n_{j+\frac{1}{2}}$, where the solution of (1.1),(1.3) with $u_0(x) = \widetilde{u}(x,t^n)$ is smooth and nonsmooth, respectively.

Given the reconstruction $\{p^n_j(x)\}$, we integrate over these domains and obtain the cell averages

$$\begin{aligned}\bar{w}^{n+1}_j = \frac{1}{x^n_{j+\frac{1}{2},l} - x^n_{j-\frac{1}{2},r}}\Bigg[&\int\limits_{x^n_{j-\frac{1}{2},r}}^{x^n_{j+\frac{1}{2},l}} p^n_j(x)\,dx\\ &- \int\limits_{t^n}^{t^{n+1}} \Big(f(u(x^n_{j+\frac{1}{2},l},t)) - f(u(x^n_{j-\frac{1}{2},r},t))\Big)\,dt\Bigg],\end{aligned} \tag{2.7}$$

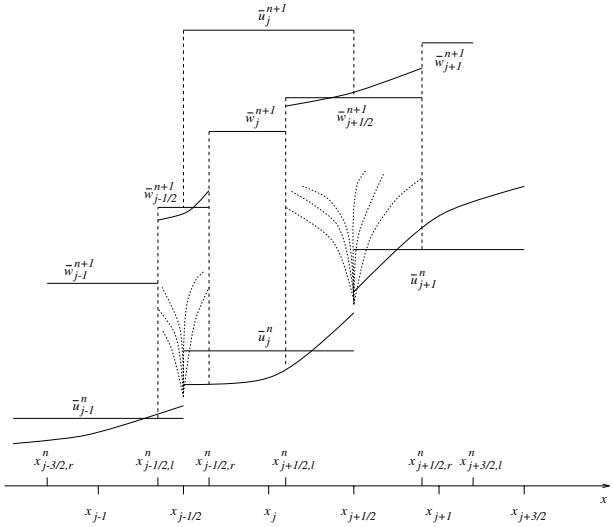


**Fig. 2.1.** Modified central differencing

and

$$\bar{w}_{j+\frac{1}{2}}^{n+1} = \frac{1}{x_{j+\frac{1}{2},r}^n - x_{j+\frac{1}{2},l}^n}\left[\int\limits_{x_{j+\frac{1}{2},l}^n}^{x_{j+\frac{1}{2}}} p_j^n(x)\,dx + \int\limits_{x_{j+\frac{1}{2}}}^{x_{j+\frac{1}{2},r}^n} p_{j+1}^n(x)\,dx\right.$$

$$\left. - \int\limits_{t^n}^{t^{n+1}} \Big(f(u(x_{j+\frac{1}{2},r}^n, t)) - f(u(x_{j+\frac{1}{2},l}^n, t))\Big)\,dt\right] \tag{2.8}$$

over the corresponding non-equal spatial cells (see Fig. 2.1).

The spatial integrals in (2.7) and (2.8) can be computed explicitly. For the approximation of the flux integrals an appropriate quadrature rule can be used, since the solution is smooth along the vertical lines $x = x_{j+\frac{1}{2},l}^n$ and $x = x_{j+\frac{1}{2},r}^n$ for $t^n \le t < t^{n+1}$. Further, for the construction of a fully-discrete scheme, we need to project the computed intermediate data $\{\bar{w}^{n+1}\}$ onto the original grid. To keep the high order of accuracy, we use another non-oscillatory piecewise polynomial reconstruction, this time over the nonuniform grid (for details see [17,16]).

We would like to emphasize that the resulting fully-discrete scheme is still Godunov-type central scheme, which does not employ any Riemann solver or characteristic decomposition. Moreover, it admits an extremely simple semi-discrete formulation, which can be achieved in the following way. We substitute $\bar{u}_j^{n+1}$ from the fully-discrete scheme in

$$\frac{d}{dt}\bar{u}_j(t) = \lim_{\Delta t \to 0} \frac{\bar{u}_j^{n+1} - \bar{u}_j^n}{\Delta t},$$

and take a limit as $\Delta t \to 0$, with $\Delta x$ fixed. This was done in [17] and [16] for the second- and the third-order schemes, respectively. Actually, in a similar way, we derive the $r$th-order semi-discrete scheme

$$\frac{d}{dt}\bar{u}_j(t) = -\frac{H_{j+\frac{1}{2}}(t) - H_{j-\frac{1}{2}}(t)}{\Delta x}, \tag{2.9}$$

with the numerical flux

$$H_{j+\frac{1}{2}}(t) := \frac{f(u^+_{j+\frac{1}{2}}(t)) + f(u^-_{j+\frac{1}{2}}(t))}{2} - \frac{a_{j+\frac{1}{2}}(t)}{2}\Big[u^+_{j+\frac{1}{2}}(t) - u^-_{j+\frac{1}{2}}(t)\Big]. \tag{2.10}$$

The intermediate values $u^{\pm}_{j+\frac{1}{2}}$ are given by

$$u^+_{j+\frac{1}{2}} := p_{j+1}(x_{j+\frac{1}{2}}), \qquad u^-_{j+\frac{1}{2}} := p_j(x_{j+\frac{1}{2}}), \tag{2.11}$$

where $\{p_j\}$ is the $r$th-order piecewise polynomial reconstruction at time $t$. We leave for the reader the details of the calculations.

*Remark 2.1* The semi-discrete scheme (2.9)–(2.11) is a system of time dependent ODEs, which can be solved by an ODE solver of an appropriate order (see the discussion in [17]).

In contrast to the staggered central schemes, described in the previous section, the semi-discrete central schemes can be *efficiently* applied to the convection-diffusion equations (1.2). The resulting scheme is

$$\frac{d}{dt}\bar{u}_j(t) = -\frac{H_{j+\frac{1}{2}}(t) - H_{j-\frac{1}{2}}(t)}{\Delta x} + \frac{Q_{j+\frac{1}{2}}(t) - Q_{j-\frac{1}{2}}(t)}{\Delta x}, \tag{2.12}$$

where $Q_{j+\frac{1}{2}}$ is a reasonable approximation to the diffusion flux at $x = x_{j+\frac{1}{2}}$ (for example, one may use a standard central differencing, see [16]).

This technique can also be directly applied to multidimensional problems if one uses the so-called 'dimension-by-dimension' approach (see [17, 16]). For instance, in the two-dimensional case, the corresponding semi-discrete scheme for the system

$$u_t + f(u)_x + g(u)_y = 0 \tag{2.13}$$

is

$$\frac{d}{dt}\bar{u}_{j,k}(t) = -\frac{H^x_{j+\frac{1}{2},k}(t) - H^x_{j-\frac{1}{2},k}(t)}{\Delta x} - \frac{H^y_{j,k+\frac{1}{2}}(t) - H^y_{j,k-\frac{1}{2}}(t)}{\Delta y}. \tag{2.14}$$

Here, the numerical fluxes are a straightforward generalization of the one-dimensional numerical flux (2.10),

$$H^x_{j+\frac{1}{2},k}(t) := \frac{f(u^+_{j+\frac{1}{2},k}(t)) + f(u^-_{j+\frac{1}{2},k}(t))}{2} - \frac{a^x_{j+\frac{1}{2},k}(t)}{2}\Big[u^+_{j+\frac{1}{2},k}(t) - u^-_{j+\frac{1}{2},k}(t)\Big], \tag{2.15}$$

and

$$H^y_{j,k+\frac{1}{2}}(t) := \frac{g(u^+_{j,k+\frac{1}{2}}(t)) + g(u^-_{j,k+\frac{1}{2}}(t))}{2} - \frac{a^y_{j,k+\frac{1}{2}}(t)}{2}\Big[u^+_{j,k+\frac{1}{2}}(t) - u^-_{j,k+\frac{1}{2}}(t)\Big]. \tag{2.16}$$

For more details, we refer the reader to [17] and [16].

In this paper (Sect. 3.2), we present an alternative *genuienly multidimensional* extension of the scheme (2.9)–(2.11), which is different from (2.14)–(2.16) for third- and higher-order schemes. Our numerical experiments demonstrate the advantage of our genuienly multidimensional construction over the straightforward 'dimension-by-dimension' approach.

### *2.3 A piecewise quadratic non-oscillatory reconstruction*

In this section, we give a brief description of the third-order non-oscillatory reconstruction of Liu and Tadmor [29]. Later on, in Sect. 3.1, we propose a new, less dissipative modification of this reconstriction.

Let us denote by $D_\pm$ and $D_0$ the one-sided and the central divided differences

$$D_\pm v(x) := \pm\frac{v(x \pm \Delta x) - v(x)}{\Delta x},$$
$$D_0 v(x) := \frac{v(x + \Delta x) - v(x - \Delta x)}{2\Delta x}.$$

We start with the basic piecewise quadratic reconstruction

$$q_j^n(x) = (\bar{u}_j^n - \frac{(\Delta x)^2}{24} D_+ D_- \bar{u}_j^n) + D_0 \bar{u}_j^n (x - x_j) + \frac{1}{2} D_+ D_- \bar{u}_j^n (x - x_j)^2, \tag{2.17}$$

which obeys the requirements of *conservation* and *accuracy*. Moreover, it satisfies a *shape-preserving* property, namely

- $q_j^n(x)$ is monotone on $(x_{j-\frac{1}{2}}, x_{j+\frac{1}{2}})$ if and only if the sequence $\bar{u}_{j-1}^n, \bar{u}_j^n, \bar{u}_{j+1}^n$ is monotone,
- $q_j^n(x)$ has extremum in the interior of $(x_{j-\frac{1}{2}}, x_{j+\frac{1}{2}})$ if and only if $\bar{u}_j^n$ is a local extremum.

This property implies that in the process of reconstruction no new extrema are created at the interior of the intervals $(x_{j-\frac{1}{2}}, x_{j+\frac{1}{2}})$. The only places where any new extrema may appear are the interface points $\{x_{j\pm\frac{1}{2}}\}$. To avoid this, one should use new quadratic polynomials $\{p_j^n\}$, which are convex combination of the basic parabolas $q_j^n$ and the cell averages $\bar{u}_j^n$, this is

$$p_j^n(x) = (1 - \theta_j^n)\bar{u}_j^n + \theta_j^n q_j^n(x), \qquad 0 < \theta_j^n < 1. \tag{2.18}$$

Here, $\theta_j^n$ are determined from the formula

$$\theta_j^n := \begin{cases} \min\left\{ \dfrac{M_{j+\frac{1}{2}}^n - \bar{u}_j^n}{M_j^n - \bar{u}_j^n}, \dfrac{m_{j-\frac{1}{2}}^n - \bar{u}_j^n}{m_j^n - \bar{u}_j^n}, 1 \right\}, & \text{if } \bar{u}_{j-1}^n < \bar{u}_j^n < \bar{u}_{j+1}^n, \\ \min\left\{ \dfrac{M_{j-\frac{1}{2}}^n - \bar{u}_j^n}{M_j^n - \bar{u}_j^n}, \dfrac{m_{j+\frac{1}{2}}^n - \bar{u}_j^n}{m_j^n - \bar{u}_j^n}, 1 \right\}, & \text{if } \bar{u}_{j-1}^n > \bar{u}_j^n > \bar{u}_{j+1}^n, \\ 1, & \text{otherwise,} \end{cases} \tag{2.19}$$

where

$$M_j^n = \max\left\{ q_j^n(x_{j+\frac{1}{2}}), q_j^n(x_{j-\frac{1}{2}}) \right\},$$
$$m_j^n = \min\left\{ q_j^n(x_{j+\frac{1}{2}}), q_j^n(x_{j-\frac{1}{2}}) \right\},$$

and

$$M_{j\pm\frac{1}{2}}^n = \max\left\{ \frac{1}{2}\left(\bar{u}_j^n + \bar{u}_{j\pm1}^n\right), q_{j\pm1}^n(x_{j\pm\frac{1}{2}}) \right\},$$
$$m_{j\pm\frac{1}{2}}^n = \min\left\{ \frac{1}{2}\left(\bar{u}_j^n + \bar{u}_{j\pm1}^n\right), q_{j\pm1}^n(x_{j\pm\frac{1}{2}}) \right\}.$$

As it was proved in [29], such a choice of the limiter $\theta_j^n$ ensures that in smooth regions $1-\theta_j^n \sim (\Delta x)^3$. Thus, the reconstruction $\{p_j^n\}$ is a third-order accurate. The polynomials $\{p_j^n\}$ also inherit the conservation and the shape-preserving properties of $\{q_j^n\}$. Moreover, the limiters $\theta_j^n$ are designed to prevent oscillations at the interface points in the sense that new extrema are created neither at the interior of the intervals $(x_{j-\frac{1}{2}}, x_{j+\frac{1}{2}})$, nor at their endpoints. We refer the reader to [29] for details.

## 3 New genuine multidimensional semi-discrete central scheme

In this section, we introduce a new semi-discrete central scheme, which is a genuine multidimensional extension of the scheme (2.9)–(2.11). It employs a multidimensional generalization (Sect. 3.4) of the new piecewise quadratic reconstruction (Sect. 3.1).

### *3.1 A new one-dimensional reconstruction*

As in Sect. 2.3 (see also [29]), we use the basic piecewise quadratic function $\{q_j^n\}$, defined in (2.17). The new reconstruction $p_j^n$ is obtained as a convex combination of $q_j^n$ and the piecewise linear interpolant $L_j^n$ ( – vs. the convex combination of $q_j^n$ and the piecewise constant function $\bar{u}_j^n$ in (2.18)),

$$p_j^n(x) = (1-\theta_j^n)L_j^n(x) + \theta_j^n q_j^n(x), \qquad 0 < \theta_j^n < 1, \tag{3.1}$$

where

$$L_j^n(x) = \bar{u}_j^n + s_j^n(x - x_j). \tag{3.2}$$

The non-oscillatory property of the new piecewise quadratic reconstruction $\{p_j^n\}$ is ensured by an appropriate choice of $\{\theta_j^n\}$ and by a non-oscillatory property of $\{L_j^n\}$ (which depends on the choice of the slopes $\{s_j^n\}$). We take $\{\theta_j^n\}$ to be

$$\theta_j^n := \begin{cases} \min\left\{\dfrac{M_{j+\frac{1}{2}}^n - L_j^n(x_{j+\frac{1}{2}})}{M_j^n - L_j^n(x_{j+\frac{1}{2}})}, \dfrac{m_{j-\frac{1}{2}}^n - L_j^n(x_{j-\frac{1}{2}})}{m_j^n - L_j^n(x_{j-\frac{1}{2}})}, 1\right\}, \\ \qquad\qquad \text{if} \quad \bar{u}_{j-1}^n < \bar{u}_j^n < \bar{u}_{j+1}^n, \\ \min\left\{\dfrac{M_{j-\frac{1}{2}}^n - L_j^n(x_{j-\frac{1}{2}})}{M_j^n - L_j^n(x_{j-\frac{1}{2}})}, \dfrac{m_{j+\frac{1}{2}}^n - L_j^n(x_{j+\frac{1}{2}})}{m_j^n - L_j^n(x_{j+\frac{1}{2}})}, 1\right\}, \\ \qquad\qquad \text{if} \quad \bar{u}_{j-1}^n > \bar{u}_j^n > \bar{u}_{j+1}^n, \\ 1, \qquad\qquad \text{otherwise}, \end{cases} \tag{3.3}$$

where

$$M_j^n = \max\left\{q_j^n(x_{j+\frac{1}{2}}), q_j^n(x_{j-\frac{1}{2}})\right\},$$
$$m_j^n = \min\left\{q_j^n(x_{j+\frac{1}{2}}), q_j^n(x_{j-\frac{1}{2}})\right\},$$

and

$$M_{j\pm\frac{1}{2}}^n = \max\left\{\frac{1}{2}\left(L_j^n(x_{j\pm\frac{1}{2}}) + L_{j\pm1}^n(x_{j\pm\frac{1}{2}})\right), q_{j\pm1}^n(x_{j\pm\frac{1}{2}})\right\},$$
$$m_{j\pm\frac{1}{2}}^n = \min\left\{\frac{1}{2}\left(L_j^n(x_{j\pm\frac{1}{2}}) + L_{j\pm1}^n(x_{j\pm\frac{1}{2}})\right), q_{j\pm1}^n(x_{j\pm\frac{1}{2}})\right\}.$$

In this paper, we use the non-oscillatory TVD *minmod* interpolant $\{L_j^n\}$, defined in (3.2),(2.5). This guarantees that the number of local extrema of $\{p_j^n\}$ does not exceed the number of extrema of $\{\bar{u}_j^n\}$ (NED property). The proof of the NED property is the same as in [29], and we omit the details. One can also easily check that our new reconstruction (3.1)–(3.3) possesses all the properties of the basic parabolas $\{q_j^n\}$ – conservation, accuracy and shape-preserving.

*Remark 3.1* The new reconstruction (3.1)–(3.3) is a less dissipative generalization of (2.17)–(2.19). This fact allows us to achieve a better resolution, as illustrated in the numerical examples in Sect. 4. At the same time, the modified reconstruction (3.1)–(3.3) is only slightly more computationally expensive than the original one.

Notice, that if one sets all slopes $s_j^n$ to be zero, then (3.1)–(3.3) is reduced to (2.17)–(2.19).

In summary, the resulting piecewise parabolic reconstruction has the form

$$p_j^n(x) = \left(\bar{u}_j^n - \theta_j^n\frac{(\Delta x)^2}{24}D_+D_-\bar{u}_j^n\right) + \left(\theta_j^n D_0\bar{u}_j^n + (1-\theta_j^n)s_j^n\right)$$
$$\times(x-x_j) + \frac{\theta_j^n}{2}D_+D_-\bar{u}_j^n(x-x_j)^2, \tag{3.4}$$

where $\theta_j^n$ and $s_j^n$ are given by (3.3) and (2.5), respectively.

### *3.2 A genuinely multidimensional approach – fully-discrete set up*

In this section, we generalize the idea of the one-dimensional construction, described in Sect. 2.1 (see Fig. 2.1) for the multidimensional case. For simplicity, we will discuss only the two-dimensional system of hyperbolic conservation laws (2.13).

Let $x_j := j\Delta x$, $y_k := k\Delta y$, $x_{j\pm\frac{1}{2}} := x_j \pm \frac{\Delta x}{2}$, $y_{k\pm\frac{1}{2}} := y_k \pm \frac{\Delta y}{2}$. Assume that at time $t = t^n$ we have already constructed a conservative piecewise polynomial interpolant of an appropriate order

$$\widetilde{u}^n(x,y) := \sum_{j,k} p^n_{j,k}(x,y)\chi_{j,k}(x,y),$$

with possible discontinuities along the interface lines $x = x_{j\pm\frac{1}{2}}$ and $y = y_{k\pm\frac{1}{2}}$. Later on, in Sect. 3.4, we present a new piecewise quadratic reconstruction, especially designed for the purposes of this scheme. We denote the corresponding point values by

$$\begin{aligned}
&u_{j,k} := p^n_{j,k}(x_j, y_k), \quad u^{\mathrm{N}}_{j,k} := p^n_{j,k}(x_j, y_{k+\frac{1}{2}}),\\
&u^{\mathrm{S}}_{j,k} := p^n_{j,k}(x_j, y_{k-\frac{1}{2}}), \quad u^{\mathrm{E}}_{j,k} := p^n_{j,k}(x_{j+\frac{1}{2}}, y_k),\\
&u^{\mathrm{W}}_{j,k} := p^n_{j,k}(x_{j-\frac{1}{2}}, y_k), \quad u^{\mathrm{NE}}_{j,k} := p^n_{j,k}(x_{j+\frac{1}{2}}, y_{k+\frac{1}{2}}),\\
&u^{\mathrm{NW}}_{j,k} := p^n_{j,k}(x_{j-\frac{1}{2}}, y_{k+\frac{1}{2}}), \quad u^{\mathrm{SE}}_{j,k} := p^n_{j,k}(x_{j+\frac{1}{2}}, y_{k-\frac{1}{2}}),\\
&u^{\mathrm{SW}}_{j,k} := p^n_{j,k}(x_{j-\frac{1}{2}}, y_{k-\frac{1}{2}}),
\end{aligned} \tag{3.5}$$

and the cell average by

$$\bar{u}_{j,k} := \frac{1}{\Delta x\Delta y}\int\limits_{x_{j-\frac{1}{2}}}^{x_{j+\frac{1}{2}}}\int\limits_{y_{k-\frac{1}{2}}}^{y_{k+\frac{1}{2}}} p^n_{j,k}(x,y)\,dxdy.$$

As in the one-dimensional case, our construction employs the CFL related maximal local speeds of propagation of the discontinuities, and we denote these speeds by $\{a^x_{j\pm\frac{1}{2},k}\}$ and $\{a^y_{j,k\pm\frac{1}{2}}\}$. They are not easy to compute, but in practice one may use, for example, the values

$$\begin{aligned}
a^x_{j+\frac{1}{2},k} &:= \max\Big\{\rho\Big(\frac{\partial f}{\partial u}(u^{\mathrm{W}}_{j+1,k})\Big), \rho\Big(\frac{\partial f}{\partial u}(u^{\mathrm{E}}_{j,k})\Big)\Big\},\\
a^y_{j,k+\frac{1}{2}} &:= \max\Big\{\rho\Big(\frac{\partial g}{\partial u}(u^{\mathrm{S}}_{j,k+1})\Big), \rho\Big(\frac{\partial g}{\partial u}(u^{\mathrm{N}}_{j,k})\Big)\Big\}.
\end{aligned} \tag{3.6}$$

Further, we consider the nonuniform domains

$$\begin{aligned}
&D_{j,k}\times[t^n,t^{n+1}], \quad D_{j\pm\frac{1}{2},k}\times[t^n,t^{n+1}],\\
&D_{j,k\pm\frac{1}{2}}\times[t^n,t^{n+1}], \quad D_{j\pm\frac{1}{2},k\pm\frac{1}{2}}\times[t^n,t^{n+1}],
\end{aligned}$$

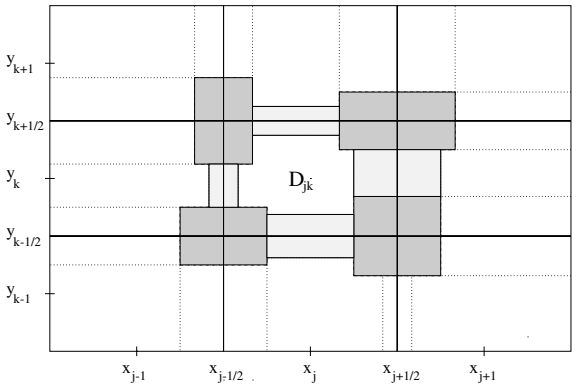


**Fig. 3.1.** Two-dimensional modified central differencing

outlined in Fig. 3.1. They are determined by the corresponding local speeds,

$$\begin{aligned}
D_{j,k+\frac{1}{2}} &:= [x_{j-\frac{1}{2}} + A^x_{j-\frac{1}{2},k+\frac{1}{2}}\Delta t,\ x_{j+\frac{1}{2}} - A^x_{j+\frac{1}{2},k+\frac{1}{2}}\Delta t]\\
&\quad\times[y_{k+\frac{1}{2}} - a^y_{j,k+\frac{1}{2}}\Delta t,\ y_{k+\frac{1}{2}} + a^y_{j,k+\frac{1}{2}}\Delta t],\\
D_{j+\frac{1}{2},k} &:= [x_{j+\frac{1}{2}} - a^x_{j+\frac{1}{2},k}\Delta t,\ x_{j+\frac{1}{2}} + a^x_{j+\frac{1}{2},k}\Delta t]\\
&\quad\times[y_{k-\frac{1}{2}} + A^y_{j+\frac{1}{2},k-\frac{1}{2}}\Delta t,\ y_{k+\frac{1}{2}} - A^y_{j+\frac{1}{2},k+\frac{1}{2}}\Delta t],\\
D_{j+\frac{1}{2},k+\frac{1}{2}} &:= [x_{j+\frac{1}{2}} - A^x_{j+\frac{1}{2},k+\frac{1}{2}}\Delta t,\ x_{j+\frac{1}{2}} + A^x_{j+\frac{1}{2},k+\frac{1}{2}}\Delta t]\\
&\quad\times[y_{k+\frac{1}{2}} - A^y_{j+\frac{1}{2},k+\frac{1}{2}}\Delta t,\ y_{k+\frac{1}{2}} + A^y_{j+\frac{1}{2},k+\frac{1}{2}}\Delta t],
\end{aligned}$$

where

$$\begin{aligned}
A^x_{j+\frac{1}{2},k+\frac{1}{2}} &:= \max\left\{a^x_{j+\frac{1}{2},k}, a^x_{j+\frac{1}{2},k+1}\right\},\\
A^y_{j+\frac{1}{2},k+\frac{1}{2}} &:= \max\left\{a^y_{j,k+\frac{1}{2}}, a^y_{j+1,k+\frac{1}{2}}\right\}.
\end{aligned}$$

Under an appropriate CFL restriction, the solution of the system (2.13), subject to the initial data $u(x,y,0) = \widetilde{u}^n(x,y)$, is smooth in $D_{j,k}$ (which is, in general, a *nonrectangular* domain inside the $(j,k)$-cell, see Fig. 3.1), and may be nonsmooth in the other domains.

Given the reconstruction $\widetilde{u}^n$, we integrate the system (2.13) over these domains, and obtain the corresponding cell averages

$$\begin{aligned}
\bar{w}^{n+1}_{j,k+\frac{1}{2}} &= \frac{1}{2a^y_{j,k+\frac{1}{2}}\Delta t\Big(\Delta x - (A^x_{j+\frac{1}{2},k+\frac{1}{2}} + A^x_{j-\frac{1}{2},k+\frac{1}{2}})\Delta t\Big)}\\
&\quad\times\Bigg(\iint\limits_{D_{j,k+\frac{1}{2}}} \widetilde{u}^n(x,y)\,dx\,dy -
\end{aligned}$$

$$
\begin{aligned}
&- \int_{t^n}^{t^{n+1}} \int_{y_{k+\frac12}-a^y_{j,k+\frac12}\Delta t}^{y_{k+\frac12}+a^y_{j,k+\frac12}\Delta t} f(u(x,y,t))\Big|_{x=x_{j-\frac12}+A^x_{j-\frac12,k+\frac12}\Delta t}^{x_{j+\frac12}-A^x_{j+\frac12,k+\frac12}\Delta t} dy\,dt - \\
&- \int_{t^n}^{t^{n+1}} \int_{x_{j-\frac12}+A^x_{j-\frac12,k+\frac12}\Delta t}^{x_{j+\frac12}-A^x_{j+\frac12,k+\frac12}\Delta t} g(u(x,y,t))\Big|_{y=y_{k+\frac12}-a^y_{j,k+\frac12}\Delta t}^{y_{k+\frac12}+a^y_{j,k+\frac12}\Delta t} dx\,dt\Bigg),
\end{aligned} \tag{3.7}
$$

$$
\begin{aligned}
\bar w^{n+1}_{j+\frac12,k} &= \frac{1}{2a^x_{j+\frac12,k}\Delta t\Big(\Delta y-(A^y_{j+\frac12,k+\frac12}+A^y_{j+\frac12,k-\frac12})\Delta t\Big)} \\
&\times\Bigg(\iint_{D_{j+\frac12,k}} \widetilde{u}^n(x,y)\,dx\,dy - \\
&- \int_{t^n}^{t^{n+1}} \int_{y_{k-\frac12}+A^y_{j+\frac12,k-\frac12}\Delta t}^{y_{k+\frac12}-A^y_{j+\frac12,k+\frac12}\Delta t} f(u(x,y,t))\Big|_{x=x_{j+\frac12}-a^x_{j+\frac12,k}\Delta t}^{x_{j+\frac12}+a^x_{j+\frac12,k}\Delta t} dy\,dt - \\
&- \int_{t^n}^{t^{n+1}} \int_{x_{j+\frac12}-a^x_{j+\frac12,k}\Delta t}^{x_{j+\frac12}+a^x_{j+\frac12,k}\Delta t} g(u(x,y,t))\Big|_{y=y_{k-\frac12}+A^y_{j+\frac12,k-\frac12}\Delta t}^{y_{k+\frac12}-A^y_{j+\frac12,k+\frac12}\Delta t} dx\,dt\Bigg),
\end{aligned} \tag{3.8}
$$

$$
\begin{aligned}
&\bar w^{n+1}_{j+\frac12,k+\frac12} \\
&= \frac{1}{4A^x_{j+\frac12,k+\frac12}A^y_{j+\frac12,k+\frac12}(\Delta t)^2}\Bigg(\iint_{D_{j+\frac12,k+\frac12}} \widetilde{u}^n(x,y)\,dx\,dy - \\
&- \int_{t^n}^{t^{n+1}} \int_{y_{k+\frac12}-A^y_{j+\frac12,k+\frac12}\Delta t}^{y_{k+\frac12}+A^y_{j+\frac12,k+\frac12}\Delta t} f(u(x,y,t))\Big|_{x=x_{j+\frac12}-A^x_{j+\frac12,k+\frac12}\Delta t}^{x_{j+\frac12}+A^x_{j+\frac12,k+\frac12}\Delta t} dy\,dt - \\
&- \int_{t^n}^{t^{n+1}} \int_{x_{j+\frac12}-A^x_{j+\frac12,k+\frac12}\Delta t}^{x_{j+\frac12}+A^x_{j+\frac12,k+\frac12}\Delta t} g(u(x,y,t))\Big|_{y=y_{k+\frac12}-A^y_{j+\frac12,k+\frac12}\Delta t}^{y_{k+\frac12}+A^y_{j+\frac12,k+\frac12}\Delta t} dx\,dt\Bigg).
\end{aligned} \tag{3.9}
$$

The computation of $\bar{w}^{n+1}_{j,k}$ is more complicated, but it can be handled in a similar way. The spatial integrals in (3.7)–(3.9) can be computed exactly and for the flux integrals one may use an appropriate quadrature formula (following the approach in [11,22]).

As in the one-dimensional case, we complete the construction of the fully-discrete scheme in two steps. We first build a new piecewise polynomial reconstruction

$$\widetilde{w}^{n+1}(x,y) := \sum_{j,k} \Bigg[ \widetilde{w}^{n+1}_{j,k} \widetilde{\chi}_{j,k} + \widetilde{w}^{n+1}_{j+\frac{1}{2},k} \widetilde{\chi}_{j+\frac{1}{2},k} + \widetilde{w}^{n+1}_{j,k+\frac{1}{2}} \widetilde{\chi}_{j,k+\frac{1}{2}} + \widetilde{w}^{n+1}_{j+\frac{1}{2},k+\frac{1}{2}} \widetilde{\chi}_{j+\frac{1}{2},k+\frac{1}{2}} \Bigg],$$

where the $\widetilde{\chi}$'s are the characteristic functions of the corresponding $D$'s. Then, we project $\widetilde{w}^{n+1}$ back onto the original grid and obtain the new cell averages

$$\bar{u}^{n+1}_{j,k} = \frac{1}{\Delta x \Delta y} \int_{x_{j-\frac{1}{2}}}^{x_{j+\frac{1}{2}}} \int_{y_{k-\frac{1}{2}}}^{y_{k+\frac{1}{2}}} \widetilde{w}^{n+1}(x,y)\, dxdy. \tag{3.10}$$

The explicit form of the resulting fully-discrete scheme is extremely complicated, and is of no practical use. Fortunately, all the computations, which have been omitted in this section, are drastically simplified if they are made in a semi-discrete context (as $\Delta t \longrightarrow 0$).

### *3.3 A genuinely multidimensional third-order semi-discrete scheme*

In this section, we derive our new genuinely multidimensional semi-discrete scheme. We proceed as in Sect. 2.2 (see also [17,16]). Using (3.10), we obtain

$$\begin{aligned} \frac{d}{dt}\bar{u}_{j,k}(t) &= \lim_{\Delta t \to 0} \frac{\bar{u}^{n+1}_{j,k} - \bar{u}^{n}_{j,k}}{\Delta t} \\ &= \lim_{\Delta t \to 0} \frac{1}{\Delta t} \left[ \frac{1}{\Delta x \Delta y} \int_{x_{j-\frac{1}{2}}}^{x_{j+\frac{1}{2}}} \int_{y_{k-\frac{1}{2}}}^{y_{k+\frac{1}{2}}} \widetilde{w}^{n+1}(x,y)\, dxdy - \bar{u}^{n}_{j,k} \right]. \end{aligned} \tag{3.11}$$

The following notation for the intersections of the cell $[x_{j-\frac{1}{2}}, x_{j+\frac{1}{2}}] \times [y_{k-\frac{1}{2}}, y_{k+\frac{1}{2}}]$ with the $D$-domains is used: $C_{j\pm\frac{1}{2},k\pm\frac{1}{2}}$ for the four corners, $S_{j\pm\frac{1}{2},k}$, $S_{j,k\pm\frac{1}{2}}$ for the four side domains and $D_{j,k}$ for the center. Notice,

that since the size of the $C$-domains is proportional to $(\Delta t)^2$, and the size of the $S$-domains $\sim \Delta t$, we have

$$\widetilde{w}^{n+1}_{j\pm\frac12,k\pm\frac12}(x,y)=\bar{w}^{n+1}_{j\pm\frac12,k\pm\frac12}+\mathcal{O}((\Delta t)^2), \tag{3.12}$$

$$\begin{aligned}\widetilde{w}^{n+1}_{j\pm\frac12,k}(x,y)&=\bar{w}^{n+1}_{j\pm\frac12,k}+\mathcal{O}(\Delta t),\\ \widetilde{w}^{n+1}_{j,k\pm\frac12}(x,y)&=\bar{w}^{n+1}_{j,k\pm\frac12}+\mathcal{O}(\Delta t),\end{aligned} \tag{3.13}$$

and due to the conservation property of the reconstruction

$$\frac{1}{|D_{j,k}|}\iint\limits_{D_{j,k}}\widetilde{w}^{n+1}_{j,k}(x,y)\,dxdy=\bar{w}^{n+1}_{j,k}. \tag{3.14}$$

The substitution of (3.12)–(3.14) in (3.11) yields

$$\begin{aligned}\frac{d}{dt}\bar{u}_{j,k}(t)=\lim_{\Delta t\to0}\frac{1}{\Delta t\Delta x\Delta y}\Bigg(&\sum_{\pm}\iint\limits_{C_{j\pm\frac12,k\pm\frac12}}\bar{w}^{n+1}_{j\pm\frac12,k\pm\frac12}\,dxdy\\ &+\sum_{\pm}\iint\limits_{S_{j,k\pm\frac12}}\bar{w}^{n+1}_{j,k\pm\frac12}\,dxdy\\ &+\sum_{\pm}\iint\limits_{S_{j\pm\frac12,k}}\bar{w}^{n+1}_{j\pm\frac12,k}\,dxdy\Bigg)\\ &+\lim_{\Delta t\to0}\frac{1}{\Delta t}\left[\frac{|D_{j,k}|}{\Delta x\Delta y}\bar{w}^{n+1}_{j,k}-\bar{u}^{n}_{j,k}\right].\end{aligned} \tag{3.15}$$

The first sum in (3.15) tends to zero as $\Delta t\to 0$, since $|C_{j\pm\frac12,k\pm\frac12}|=\mathcal{O}((\Delta t)^2)$. To pass to the limit in the second sum, we use the fact that $|S_{j,k+\frac12}|=a^y_{j,k+\frac12}\Delta t\Delta x+\mathcal{O}((\Delta t)^2)$, and obtain

$$\lim_{\Delta t\to0}\frac{1}{\Delta t\Delta x\Delta y}\iint\limits_{S_{j,k+\frac12}}\bar{w}^{n+1}_{j,k+\frac12}\,dxdy=\frac{a^y_{j,k+\frac12}}{\Delta y}\lim_{\Delta t\to0}\bar{w}^{n+1}_{j,k+\frac12}. \tag{3.16}$$

It follows from (3.7) that the value of $\lim\limits_{\Delta t\to0}\bar{w}^{n+1}_{j,k+\frac12}$ is

$$\frac{1}{2\Delta x}\left[\int\limits_{x_{j-\frac12}}^{x_{j+\frac12}}\Big\{p^n_{j,k+1}(x,y_{k+\frac12})+p^n_{j,k}(x,y_{k+\frac12})\right.$$

$$-\frac{g(p^n_{j,k+1}(x,y_{k+\frac12}))-g(p^n_{j,k}(x,y_{k+\frac12}))}{a^y_{j,k+\frac12}}\Big\}\,dx\Bigg].$$

We then apply the Simpson's quadrature formula to the above integral, and using (3.16), we arrive at

$$\begin{aligned}
&\lim_{\Delta t\to 0}\frac{1}{\Delta t\Delta x\Delta y}\iint\limits_{S_{j,k+\frac12}}\bar w^{n+1}_{j,k+\frac12}\,dxdy\\
&\quad\approx\frac{a^y_{j,k+\frac12}}{12\Delta y}\Big[u^{\mathrm{SW}}_{j,k+1}+u^{\mathrm{NW}}_{j,k}+4(u^{\mathrm{S}}_{j,k+1}+u^{\mathrm{N}}_{j,k})+u^{\mathrm{SE}}_{j,k+1}+u^{\mathrm{NE}}_{j,k}\Big]\\
&\qquad-\frac{1}{12\Delta y}\Big[g(u^{\mathrm{SW}}_{j,k+1})-g(u^{\mathrm{NW}}_{j,k})+4(g(u^{\mathrm{S}}_{j,k+1})-g(u^{\mathrm{N}}_{j,k}))\\
&\qquad+g(u^{\mathrm{SE}}_{j,k+1})-g(u^{\mathrm{NE}}_{j,k})\Big].
\end{aligned}\tag{3.17}$$

A similar treatment of the third sum in (3.15) leads to

$$\begin{aligned}
&\lim_{\Delta t\to 0}\frac{1}{\Delta t\Delta x\Delta y}\iint\limits_{S_{j+\frac12,k}}\bar w^{n+1}_{j+\frac12,k}\,dxdy\\
&\quad\approx\frac{a^x_{j+\frac12,k}}{12\Delta x}\Big[u^{\mathrm{NW}}_{j+1,k}+u^{\mathrm{NE}}_{j,k}+4(u^{\mathrm{W}}_{j+1,k}+u^{\mathrm{E}}_{j,k})+u^{\mathrm{SW}}_{j+1,k}+u^{\mathrm{SE}}_{j,k}\Big]\\
&\qquad-\frac{1}{12\Delta x}\Big[f(u^{\mathrm{NW}}_{j+1,k})-f(u^{\mathrm{NE}}_{j,k})+4(f(u^{\mathrm{W}}_{j+1,k})-f(u^{\mathrm{E}}_{j,k}))\\
&\qquad+f(u^{\mathrm{SW}}_{j+1,k})-f(u^{\mathrm{SE}}_{j,k})\Big].
\end{aligned}\tag{3.18}$$

Finally, we consider the last term in (3.15). Note, that in the limit as $\Delta t\to 0$, the domain $D_{j,k}$ becomes *rectangular*, up to small corners of a negligible size $\mathcal{O}((\Delta t)^2)$ (see Fig. 3.1), and thus one can easily integrate equation (2.13) over $D_{j,k}\times[t^n,t^n+\Delta t]$. This observation together with Simpson's rule give

$$\begin{aligned}
&\lim_{\Delta t\to 0}\frac{1}{\Delta t}\left[\frac{|D_{j,k}|}{\Delta x\Delta y}\bar w^{n+1}_{j,k}-\bar u^n_{j,k}\right]\\
&\quad\approx-\frac{a^x_{j+\frac12,k}}{6\Delta x}\Big[u^{\mathrm{NE}}_{j,k}+4u^{\mathrm{E}}_{j,k}+u^{\mathrm{SE}}_{j,k}\Big]-\frac{a^x_{j-\frac12,k}}{6\Delta x}\Big[u^{\mathrm{NW}}_{j,k}+4u^{\mathrm{W}}_{j,k}+u^{\mathrm{SW}}_{j,k}\Big]\\
&\qquad-\frac{a^y_{j,k+\frac12}}{6\Delta y}\Big[u^{\mathrm{NW}}_{j,k}+4u^{\mathrm{N}}_{j,k}+u^{\mathrm{NE}}_{j,k}\Big]-\frac{a^y_{j,k-\frac12}}{6\Delta y}\Big[u^{\mathrm{SW}}_{j,k}+4u^{\mathrm{S}}_{j,k}+u^{\mathrm{SE}}_{j,k}\Big]\\
&\qquad-\frac{1}{6\Delta x}\Big[f(u^{\mathrm{NE}}_{j,k})-f(u^{\mathrm{NW}}_{j,k})+4(f(u^{\mathrm{E}}_{j,k})-f(u^{\mathrm{W}}_{j,k}))
\end{aligned}$$

$$+f(u^{\mathrm{SE}}_{j,k})-f(u^{\mathrm{SW}}_{j,k})\Big]-\frac{1}{6\Delta y}\Big[g(u^{\mathrm{NW}}_{j,k})-g(u^{\mathrm{SW}}_{j,k})+4(g(u^{\mathrm{N}}_{j,k})$$

$$-g(u^{\mathrm{S}}_{j,k}))+g(u^{\mathrm{NE}}_{j,k})-g(u^{\mathrm{SE}}_{j,k})\Big]. \tag{3.19}$$

At the end, plugging (3.17)–(3.19) into (3.15), we arrive at our new semi-discrete scheme, which can be presented in the conservative form

$$\begin{aligned}\frac{d}{dt}\bar{u}_{j,k}(t)=&-\frac{H^x_{j+\frac12,k}(t)-H^x_{j-\frac12,k}(t)}{\Delta x}\\ &-\frac{H^y_{j,k+\frac12}(t)-H^y_{j,k-\frac12}(t)}{\Delta y},\end{aligned} \tag{3.20}$$

with the numerical fluxes

$$\begin{aligned}H^x_{j+\frac12,k}(t):=&\Big\{f(u^{\mathrm{NW}}_{j+1,k}(t))+f(u^{\mathrm{NE}}_{j,k}(t))+4(f(u^{\mathrm{W}}_{j+1,k}(t))+f(u^{\mathrm{E}}_{j,k}(t)))\\ &+f(u^{\mathrm{SW}}_{j+1,k}(t))+f(u^{\mathrm{SE}}_{j,k}(t))\Big\}\Big/\Big\{12\Big\}-\frac{a^x_{j+\frac12,k}(t)}{12}\\ &\times\Big[u^{\mathrm{NW}}_{j+1,k}(t)-u^{\mathrm{NE}}_{j,k}(t)+4(u^{\mathrm{W}}_{j,k+1}(t)-u^{\mathrm{E}}_{j,k}(t))\\ &+u^{\mathrm{SW}}_{j+1,k}(t)-u^{\mathrm{SE}}_{j,k}(t)\Big],\end{aligned} \tag{3.21}$$

and

$$\begin{aligned}H^y_{j,k+\frac12}(t):=&\Big\{g(u^{\mathrm{SW}}_{j,k+1}(t))+g(u^{\mathrm{NW}}_{j,k}(t))+4(g(u^{\mathrm{S}}_{j,k+1}(t))+g(u^{\mathrm{N}}_{j,k}(t)))\\ &+g(u^{\mathrm{SE}}_{j,k+1}(t))+g(u^{\mathrm{NE}}_{j,k}(t))\Big\}\Big/\Big\{12\Big\}-\frac{a^y_{j,k+\frac12}(t)}{12}\\ &\times\Big[u^{\mathrm{SW}}_{j,k+1}(t)-u^{\mathrm{NW}}_{j,k}(t)+4(u^{\mathrm{S}}_{j,k+1}(t)-u^{\mathrm{N}}_{j,k}(t))\\ &+u^{\mathrm{SE}}_{j,k+1}(t)-u^{\mathrm{NE}}_{j,k}(t)\Big].\end{aligned} \tag{3.22}$$

Here, $a^x_{j+\frac12,k}(t)$, $a^y_{j,k+\frac12}(t)$ are given in (3.6), and the $u$'s are determined by the corresponding values of the piecewise quadratic reconstruction $\{p_{j,k}\}$ at time $t$, see (3.5).

*Remark 3.2* 1. We would like to point out that the scheme (3.20)–(3.22) has been constructed as a genuinely two-dimensional Godunov-type central scheme. Our numerical experiments demonstrate that it has sharper resolution, in comparison to the 'dimension-by-dimension' third-order central semi-discrete scheme in [16].

At the same time, our new scheme enjoys all the main advantages of central schemes, the most important of which is *simplicity*. Namely, it does not involve Riemann solvers and does not require any information about the eigenstructure of the Jacobians $\frac{\partial f}{\partial u}$ and $\frac{\partial g}{\partial u}$ beyond the CFL-related local speeds $\{a^x_{j+\frac12,k}\}$ and $\{a^y_{j,k+\frac12}\}$.

2. If in the derivation of (3.20)–(3.22), we use piecewise linear reconstruction and the second-order midpoint rule (instead of Simpson's rule), we arrive exactly at the scheme (2.14)–(2.16), obtained in [17], where the 'dimension-by-dimension' approach was used.

3. The scheme (3.20) can be generalized for the convection-diffusion equation

$$u_t + f(u)_x + g(u)_y = Q^x(u, u_x, u_y)_x + Q^y(u, u_x, u_y)_y,$$

as follows

$$\begin{aligned}\frac{d}{dt}\bar u_{j,k}(t) = &-\frac{H^x_{j+\frac12,k} - H^x_{j-\frac12,k}}{\Delta x} - \frac{H^y_{j,k+\frac12} - H^y_{j,k-\frac12}}{\Delta y}\\ &+\frac{Q^x_{j+\frac12,k} - Q^x_{j-\frac12,k}}{\Delta x} + \frac{Q^y_{j,k+\frac12} - Q^y_{j,k-\frac12}}{\Delta y}.\end{aligned} \tag{3.23}$$

Here, the numerical convection fluxes $H^x$, $H^y$ are given by (3.21),(3.22) and, as in the one-dimensional case, $Q^x_{j+\frac12,k}$ and $Q^y_{j,k+\frac12}$ are appropriate approximations to the diffusion fluxes.

4. Our semi-discrete approach can be easily extended to the multidimensional case, $d \ge 3$.

### *3.4 A new two-dimensional reconstruction via "dimension-by-dimension" approach*

We generalize the idea from Sect. 3.1 for the two-dimensional case – we construct a piecewise quadratic reconstruction $\{p^n_{j,k}\}$ as a convex combination of the basic parabolas $\{q^n_{j,k}\}$ and the linear functions $\{L^n_{j,k}\}$. The basic parabolas are given by

$$\begin{aligned}q^n_{j,k}(x,y) = &\Big(\bar u^n_{j,k} - \frac{(\Delta x)^2}{24} D^x_+ D^x_- \bar u^n_{j,k} - \frac{(\Delta y)^2}{24} D^y_+ D^y_- \bar u^n_{j,k}\Big)\\ &+D^x_0 \bar u^n_{j,k}(x - x_j) + D^y_0 \bar u^n_{j,k}(y - y_k)\\ &+\frac12 D^x_+ D^x_- \bar u^n_{j,k}(x - x_j)^2 + D^x_0 D^y_0 \bar u^n_{j,k}(x - x_j)(y - y_k)\\ &+\frac12 D^y_+ D^y_- \bar u^n_{j,k}(y - y_k)^2,\end{aligned} \tag{3.24}$$

where the corresponding divided differences are

$$D^x_{\pm}v(x,y) := \pm\frac{v(x\pm\Delta x,y)-v(x,y)}{\Delta x},$$
$$D^y_{\pm}v(x,y) := \pm\frac{v(x,y\pm\Delta y)-v(x,y)}{\Delta y},$$
$$D^x_0 v(x,y) := \frac{v(x+\Delta x,y)-v(x-\Delta x,y)}{2\Delta x},$$
$$D^y_0 v(x,y) := \frac{v(x,y+\Delta y)-v(x,y-\Delta y)}{2\Delta y}.$$

One can easily check that, as in the one-dimensional case, these parabolas satisfy the requirements of conservation and accuracy.

The piecewise linear functions have the form

$$L^n_{j,k}(x,y) = \bar{u}^n_{j,k} + s^x_{j,k}(x-x_j) + s^y_{j,k}(y-y_k), \tag{3.25}$$

where the slopes $\{s^x_{j,k}, s^y_{j,k}\}$ may be computed, for example, using the minmod limiter

$$s^x_{j,k} = \operatorname{minmod}\left(\frac{\bar{u}^n_{j,k}-\bar{u}^n_{j-1,k}}{\Delta x}, \frac{\bar{u}^n_{j+1,k}-\bar{u}^n_{j,k}}{\Delta x}\right),$$
$$s^y_{j,k} = \operatorname{minmod}\left(\frac{\bar{u}^n_{j,k}-\bar{u}^n_{j,k-1}}{\Delta y}, \frac{\bar{u}^n_{j,k+1}-\bar{u}^n_{j,k}}{\Delta y}\right). \tag{3.26}$$

Then the reconstruction is

$$p^n_{j,k}(x,y) = (1-\theta^n_{j,k})L^n_{j,k}(x,y) + \theta^n_{j,k}q^n_{j,k}(x,y),$$
$$0<\theta^n_{j,k}<1. \tag{3.27}$$

In general, the purpose of the limiters $\{\theta^n_{j,k}\}$ is to guarantee a non-oscillatory nature of the reconstruction (3.27). Unfortunately, in the two-dimensional case, we do not know how such $\theta$'s can be chosen. Moreover, it is not even clear what the definition of a non-oscillatory propery should be.

Notice, that we do not need to recover the whole reconstruction – only the eight point values $u^{\mathrm{N}}_{j,k}$, $u^{\mathrm{E}}_{j,k}$, $u^{\mathrm{S}}_{j,k}$, $u^{\mathrm{W}}_{j,k}$,$u^{\mathrm{NE}}_{j,k}$, $u^{\mathrm{NW}}_{j,k}$, $u^{\mathrm{SE}}_{j,k}$, and $u^{\mathrm{SW}}_{j,k}$ in each $(j,k)$-cell are required to compute the numerical fluxes in (3.21)–(3.22). These values may be computed using the 'dimension-by-dimension' approach, applied in two steps.

First, we use the reconstruction (3.24)–(3.27) with

$$\theta^n_{j,k} = \min\{\theta^x_{j,k}, \theta^y_{j,k}\}, \tag{3.28}$$

to compute the point values in the coordinate directions – $u^{\mathrm{N}}_{j,k}$, $u^{\mathrm{E}}_{j,k}$, $u^{\mathrm{S}}_{j,k}$ and $u^{\mathrm{W}}_{j,k}$ (see Fig. 3.2). The limiters $\{\theta^x_{j,k}\}$ and $\{\theta^y_{j,k}\}$ are determined by (3.3) with

$$L^n_j(\cdot) = L^n_{j,k}(\cdot,y_k), \qquad q_j(\cdot) = q^n_{j,k}(\cdot,y_k),$$

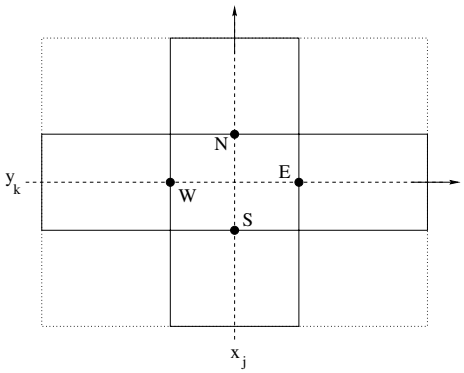


**Fig. 3.2.** Reconstruction in $x$- and $y$-directions

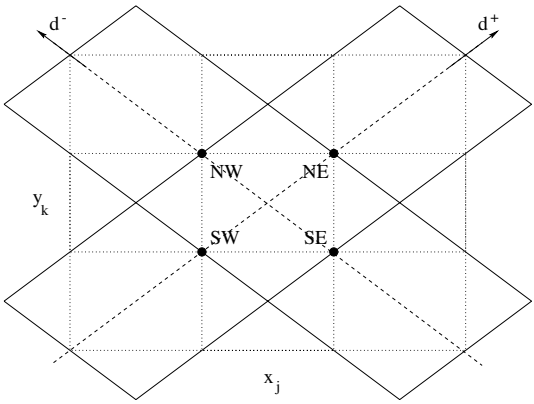


**Fig. 3.3.** Reconstruction in the diagonal directions

and

$$L_j^n(\cdot) = L_{j,k}^n(x_k, \cdot), \qquad q_j^n(\cdot) = L_{j,k}^n(x_k, \cdot).$$

The choice of $\{\theta_{j,k}^n\}$ is based on the one-dimensional non-oscillatory reconstruction, described in Sect. 3.1. This guarantees the third-order accuracy and the lack of oscillations in the $x$- and $y$-directions.

To ensure that there are no oscillations in the diagonal directions, the point values $u_{j,k}^{\mathrm{NE}}$, $u_{j,k}^{\mathrm{NW}}$, $u_{j,k}^{\mathrm{SE}}$ and $u_{j,k}^{\mathrm{SW}}$ should be computed by another reconstruction (see Fig. 3.3). This additional reconstruction is determined as a convex combination of different basic parabolas $\{\hat{q}_{j,k}^n\}$ and linear functions $\{\hat{L}_{j,k}^n\}$, adjusted to the diagonal directions $d^-$ and $d^+$,

$$\hat{p}_{j,k}^n(x,y) = (1-\hat{\theta}_{j,k}^n)\hat{L}_{j,k}^n(x,y) + \hat{\theta}_{j,k}^n \hat{q}_{j,k}^n(x,y),$$

$$0 < \hat{\theta}_{j,k}^n < 1. \tag{3.29}$$

The adjusted basic parabolas are

$$\begin{aligned}\hat{q}^n_{j,k}(x,y) = &\Big(\bar{u}^n_{j,k} - \frac{\Delta^2}{48} D^{d+}_{+} D^{d+}_{-} \bar{u}^n_{j,k} - \frac{\Delta^2}{48} D^{d-}_{+} D^{d-}_{-} \bar{u}^n_{j,k}\Big)\\ &+D^{d+}_0 \bar{u}^n_{j,k}\Big[\frac{\Delta}{2\Delta y}(y-y_k) + \frac{\Delta}{2\Delta x}(x-x_j)\Big]\\ &+D^{d-}_0 \bar{u}^n_{j,k}\Big[\frac{\Delta}{2\Delta y}(y-y_k) - \frac{\Delta}{2\Delta x}(x-x_j)\Big]\\ &+D^{d+}_0 D^{d-}_0 \bar{u}^n_{j,k}\Big[\frac{\Delta^2}{4(\Delta y)^2}(y-y_k)^2 - \frac{\Delta^2}{4(\Delta x)^2}(x-x_j)^2\Big]\\ &+\frac{1}{2} D^{d+}_{+} D^{d+}_{-} \bar{u}^n_{j,k}\Big[\frac{\Delta}{2\Delta y}(y-y_k) + \frac{\Delta}{2\Delta x}(x-x_j)\Big]^2\\ &+\frac{1}{2} D^{d-}_{+} D^{d-}_{-} \bar{u}^n_{j,k}\Big[\frac{\Delta}{2\Delta y}(y-y_k) - \frac{\Delta}{2\Delta x}(x-x_j)\Big]^2,\end{aligned} \tag{3.30}$$

where $\Delta := \sqrt{(\Delta x)^2 + (\Delta y)^2}$, and the divided differences in the diagonal directions are

$$\begin{aligned}D^{d+}_{\pm} v(x,y) &:= \pm\frac{v(x \pm \Delta x, y \pm \Delta y) - v(x,y)}{\Delta},\\ D^{d+}_{0} v(x,y) &:= \frac{v(x+\Delta x, y+\Delta y) - v(x-\Delta x, y-\Delta y)}{2\Delta},\\ D^{d-}_{\pm} v(x,y) &:= \pm\frac{v(x \mp \Delta x, y \pm \Delta y) - v(x,y)}{\Delta},\\ D^{d-}_{0} v(x,y) &:= \frac{v(x-\Delta x, y+\Delta y) - v(x+\Delta x, y-\Delta y)}{2\Delta}.\end{aligned}$$

The corresponding linear functions are given by

$$\begin{aligned}\hat{L}^n_{j,k}(x,y) = \bar{u}^n_{j,k} &+ \hat{s}^+_{j,k}\Big[\frac{\Delta}{2\Delta y}(y-y_k) + \frac{\Delta}{2\Delta x}(x-x_j)\Big]\\ &+\hat{s}^-_{j,k}\Big[\frac{\Delta}{2\Delta y}(y-y_k) - \frac{\Delta}{2\Delta x}(x-x_j)\Big],\end{aligned} \tag{3.31}$$

where the slopes are computed using the minmod limiter, applied in the diagonal directions, that is,

$$\hat{s}^+_{j,k} = \operatorname{minmod}\left(\frac{\bar{u}^n_{j,k} - \bar{u}^n_{j-1,k-1}}{\Delta}, \frac{\bar{u}^n_{j+1,k+1} - \bar{u}^n_{j,k}}{\Delta}\right), \tag{3.32}$$

$$\hat{s}^-_{j,k} = \operatorname{minmod}\left(\frac{\bar{u}^n_{j,k} - \bar{u}^n_{j+1,k-1}}{\Delta}, \frac{\bar{u}^n_{j-1,k+1} - \bar{u}^n_{j,k}}{\Delta}\right). \tag{3.33}$$

The parameter $\hat{\theta}^n_{j,k}$ in (3.29) is determined by

$$\hat{\theta}^n_{j,k} = \min\{\hat{\theta}^+_{j,k}, \hat{\theta}^-_{j,k}\}, \tag{3.34}$$

where $\hat{\theta}^+_{j,k}$ and $\hat{\theta}^-_{j,k}$ are designed to prevent oscillations in the diagonal directions $d^+$ and $d^-$, respectively. The $\hat{\theta}$'s are computed similarly to (3.3), namely

$$
\theta^{\pm}_{j,k} := \begin{cases}
\min\left\{\dfrac{M^{\pm}_{j\pm\frac12,k+\frac12} - \hat{L}^n_{j,k}(x_{j\pm\frac12}, y_{k+\frac12})}{M^{\pm}_{j,k} - \hat{L}^n_{j,k}(x_{j\pm\frac12}, y_{k+\frac12})},\right. \\
\qquad \left.\dfrac{m^{\pm}_{j\mp\frac12,k-\frac12} - \hat{L}^n_{j,k}(x_{j\mp\frac12}, y_{k-\frac12})}{m^{\pm}_{j,k} - \hat{L}^n_{j,k}(x_{j\mp\frac12}, y_{k-\frac12})}, 1\right\}, \\
\qquad \text{if} \quad \bar{u}^n_{j\mp1,k-1} < \bar{u}^n_{j,k} < \bar{u}^n_{j\pm1,k+1}, \\
\min\left\{\dfrac{M^{\pm}_{j\mp\frac12,k-\frac12} - \hat{L}^n_{j,k}(x_{j\mp\frac12}, y_{k-\frac12})}{M^{\pm}_{j,k} - \hat{L}^n_{j,k}(x_{j\mp\frac12}, y_{k-\frac12})},\right. \\
\qquad \left.\dfrac{m^{\pm}_{j\pm\frac12,k+\frac12} - \hat{L}^n_{j,k}(x_{j\pm\frac12}, y_{k+\frac12})}{m^{\pm}_{j,k} - \hat{L}^n_{j,k}(x_{j\pm\frac12}, y_{k+\frac12})}, 1\right\}, \\
\qquad \text{if} \quad \bar{u}^n_{j\mp1,k-1} > \bar{u}^n_{j,k} > \bar{u}^n_{j\pm1,k+1}, \\
1, \qquad \text{otherwise},
\end{cases} \tag{3.35}
$$

where

$$
\begin{aligned}
M^{\pm}_{j,k} &= \max\left\{\hat{q}^n_{j,k}(x_{j\pm\frac12}, y_{k+\frac12}), \hat{q}^n_{j,k}(x_{j\mp\frac12}, y_{k-\frac12})\right\}, \\
m^{\pm}_{j,k} &= \min\left\{\hat{q}^n_{j,k}(x_{j\pm\frac12}, y_{k+\frac12}), \hat{q}^n_{j,k}(x_{j\mp\frac12}, y_{k-\frac12})\right\},
\end{aligned}
$$

and

$$
\begin{aligned}
M^{+}_{j\pm\frac12,k\pm\frac12} &= \max\left\{\frac12\left(\hat{L}^n_{j,k}(x_{j\pm\frac12}, y_{k\pm\frac12}) + \hat{L}^n_{j\pm1,k\pm1}(x_{j\pm\frac12}, y_{k\pm\frac12})\right),\right. \\
&\qquad \left.\hat{q}^n_{j\pm1,k\pm1}(x_{j\pm\frac12}, y_{k\pm\frac12})\right\}, \\
m^{+}_{j\pm\frac12,k\pm\frac12} &= \min\left\{\frac12\left(\hat{L}^n_{j,k}(x_{j\pm\frac12}, y_{k\pm\frac12}) + \hat{L}^n_{j\pm1,k\pm1}(x_{j\pm\frac12}, y_{k\pm\frac12})\right),\right. \\
&\qquad \left.\hat{q}^n_{j\pm1,k\pm1}(x_{j\pm\frac12}, y_{k\pm\frac12})\right\}, \\
M^{-}_{j\mp\frac12,k\pm\frac12} &= \max\left\{\frac12\left(\hat{L}^n_{j,k}(x_{j\mp\frac12}, y_{k\pm\frac12}) + \hat{L}^n_{j\mp1,k\pm1}(x_{j\mp\frac12}, y_{k\pm\frac12})\right),\right. \\
&\qquad \left.\hat{q}^n_{j\mp1,k\pm1}(x_{j\mp\frac12}, y_{k\pm\frac12})\right\}, \\
m^{-}_{j\mp\frac12,k\pm\frac12} &= \min\left\{\frac12\left(\hat{L}^n_{j,k}(x_{j\mp\frac12}, y_{k\pm\frac12}) + \hat{L}^n_{j\mp1,k\pm1}(x_{j\mp\frac12}, y_{k\pm\frac12})\right),\right.
\end{aligned}
$$

$$\hat{q}^n_{j\mp1,k\pm1}(x_{j\mp\frac{1}{2}},y_{k\pm\frac{1}{2}})\Big\}.$$

*Remark 3.3* 1. Direct calculations show that the reconstruction $\hat{p}^n_{j,k}(x,y)$ conserves the original cell averages, that is

$$\frac{1}{\Delta x\Delta y}\int\limits_{x_{j-\frac{1}{2}}}^{x_{j+\frac{1}{2}}}\int\limits_{y_{k-\frac{1}{2}}}^{y_{k+\frac{1}{2}}}\hat{p}^n_{j,k}(x,y)\,dx\,dy=\bar{u}^n_{j,k}.$$

2. We would like to emphasize that we have actually used two different piecewise quadratic reconstructions, (3.24)–(3.28) and (3.29)–(3.35), in order to compute the eight point values along the inner boundary of the $(j,k)$-cell. In the derivation of our genuinely two-dimensional scheme (3.20)–(3.22) we use Simpson's rule, which is applied to a single smooth function, defined on the $(j,k)$-cell. For example, this smooth function can be viewed as the following convex combination,

$$(1-\varphi(x,y))p^n_{j,k}(x,y)+\varphi(x,y)\hat{p}^n_{j,k}(x,y),$$

where the weight function $\varphi$ can be any smooth function satisfying

$$\begin{aligned}\varphi(x_{j\pm\frac{1}{2}},y_k)=\varphi(x_j,y_{k\pm\frac{1}{2}})=1,\\ \varphi(x_{j\pm\frac{1}{2}},y_{k\pm\frac{1}{2}})=0,\quad 0\le\varphi(x,y)\le1.\end{aligned}$$

In summary, the values $u^{\rm N}_{j,k}$, $u^{\rm S}_{j,k}$, $u^{\rm E}_{j,k}$ and $u^{\rm W}_{j,k}$ are computed as the corresponding point values of

$$\begin{aligned}&p^n_{j,k}(x,y)\\&=\Big(\bar{u}^n_{j,k}-\theta^n_{j,k}\frac{(\Delta x)^2}{24}D^x_+D^x_-\bar{u}^n_{j,k}-\theta^n_{j,k}\frac{(\Delta y)^2}{24}D^y_+D^y_-\bar{u}^n_{j,k}\Big)\\&\quad+\Big(\theta^n_{j,k}D^x_0\bar{u}^n_{j,k}+(1-\theta^n_{j,k})s^x_{j,k}\Big)(x-x_j)\\&\quad+\Big(\theta^n_{j,k}D^y_0\bar{u}^n_{j,k}+(1-\theta^n_{j,k})s^y_{j,k}\Big)(y-y_k)\\&\quad+\frac{\theta^n_{j,k}}{2}D^x_+D^x_-\bar{u}^n_{j,k}(x-x_j)^2+\theta^n_{j,k}D^x_0D^y_0\bar{u}^n_{j,k}(x-x_j)(y-y_k)\\&\quad+\frac{\theta^n_{j,k}}{2}D^y_+D^y_-\bar{u}^n_{j,k}(y-y_k)^2,\end{aligned}\tag{3.36}$$

where $\theta^n_{j,k}$, $s^x_{j,k}$ and $s^y_{j,k}$ are given by (3.28) and (3.26), respectively. To evaluate the corner values $u^{\rm NE}_{j,k}$, $u^{\rm NW}_{j,k}$, $u^{\rm SE}_{j,k}$ and $u^{\rm SW}_{j,k}$, we use

$$\hat{p}^n_{j,k}(x,y)$$

$$
\begin{aligned}
&= \Big(\bar{u}^n_{j,k} - \hat{\theta}^n_{j,k}\frac{\Delta^2}{48}(D^{d^+}_+ D^{d^+}_- + D^{d^-}_+ D^{d^-}_-)\bar{u}^n_{j,k}\Big)\\
&+\frac{\Delta}{2\Delta x}\Big(\hat{\theta}^n_{j,k}(D^{d^+}_0 - D^{d^-}_0)\bar{u}^n_{j,k} + (1-\hat{\theta}^n_{j,k})(\hat{s}^+_{j,k} - \hat{s}^-_{j,k})\Big)(x-x_j)\\
&+\frac{\Delta}{2\Delta y}\Big(\hat{\theta}^n_{j,k}(D^{d^+}_0 + D^{d^-}_0)\bar{u}^n_{j,k} + (1-\hat{\theta}^n_{j,k})(\hat{s}^+_{j,k} + \hat{s}^-_{j,k})\Big)(y-y_k)\\
&+\hat{\theta}^n_{j,k}\frac{\Delta^2}{8(\Delta x)^2}\Big(D^{d^+}_+ D^{d^+}_- - 2D^{d^+}_0 D^{d^-}_0 + D^{d^-}_+ D^{d^-}_-\Big)\bar{u}^n_{j,k}(x-x_j)^2\\
&+\hat{\theta}^n_{j,k}\frac{\Delta^2}{4\Delta x\Delta y}\Big(D^{d^+}_+ D^{d^+}_- - D^{d^-}_+ D^{d^-}_-\Big)\bar{u}^n_{j,k}(x-x_j)(y-y_k)\\
&+\hat{\theta}^n_{j,k}\frac{\Delta^2}{8(\Delta y)^2}\Big(D^{d^+}_+ D^{d^+}_- + 2D^{d^+}_0 D^{d^-}_0 + D^{d^-}_+ D^{d^-}_-\Big)\bar{u}^n_{j,k}(y-y_k)^2, \qquad (3.37)
\end{aligned}
$$

with $\hat{\theta}^n_{j,k}$, $\hat{s}^+_{j,k}$ and $\hat{s}^-_{j,k}$, given by (3.34), (3.32) and (3.33), respectively.

## 4 Numerical examples

In this section, we present a number of numerical experiments that have been performed using the one-dimensional scheme (2.9)–(2.11) together with the new reconstruction (3.4), and our genuinely two-dimensional scheme (3.20)–(3.22), coupled with the new piecewise quadratic reconstruction (3.36), (3.37).

The third-order semi-discrete methods, presented in this paper, require at least a third-order time discretization scheme. In the numerical examples, shown below, we have used the third-order TVD Runge-Kutta method, proposed in [34, 36]. Our choice is based on the stability properties of this method, each time step of which can be viewed as a convex combination of small forward Euler steps.

To solve problem (1.2), we may use either an implicit or an explicit time discretization for the parabolic term. To ensure stability of the explicit method, an additional restriction on the time step is imposed by the parabolic term, namely $\Delta t$ must be proportional to $(\Delta x)^2$. One may accelerate the computations by using an implicit, or explicit-implicit ODE solver. These methods are unconditionally stable, but they require inverting of nonlinear operators (in the case of nonlinear diffusion), which is a computationally expensive and analytically complicated procedure. Alternatively, the acceleration may be achieved by employing an efficient explicit Runge-Kutta type ODE solver with larger stability domain (in comparison with the standard Runge-Kutta methods), see [30] and the references therein.

In all the numerical experiments below, the CFL number is equal to 0.475.

*4.1 Linear accuracy tests*

*Example 1 – One-dimensional transport equation.* First, we test the accuracy of the scheme (2.9)–(2.11) with the reconstruction (3.4) on the initial boundary value problem (IBVP) for the linear transport equation

$$\begin{cases} u_t + u_x = 0, \quad x \in [0, 2\pi], \\ u(x,0) = \sin x, \end{cases} \tag{4.1}$$

with periodic boundary conditions. This problem has a global classical solution, which is computed at time $T = 1$. We consider $N$ grid points, $N = 40, 80, \ldots, 1280$, and measure the $L^1$- and $L^\infty$-errors, respectively. To calculate the errors, we use the computed values $\{\bar{u}_j\}$ at the final time, and the sliding averages $\{\bar{u}(x_j, 1)\}$ of the exact solution of (4.1), namely

$$\|\bar{u} - \bar{u}(\cdot,1)\|_{L^1} := \Delta x \sum_j |\bar{u}_j - \bar{u}(x_j,1)|,$$
$$\|\bar{u} - \bar{u}(\cdot,1)\|_{L^\infty} := \max_j |\bar{u}_j - \bar{u}(x_j,1)|.$$

The results of these computations are presented in Table 4.1. They clearly demonstrate that the scheme is third-order.

*Example 2 – Two-dimensional transport equation.* Second, we apply our two-dimensional scheme (3.20)–(3.22) with the reconstruction (3.36)–(3.37) to the IBVP for the two-dimensional linear transport equation

$$\begin{cases} u_t + u_x + u_y = 0, \quad (x,y) \in [0,2] \times [0,1], \\ u(x,y,0) = \sin[\pi(x+2y)], \end{cases} \tag{4.2}$$

subject to periodic boundary conditions. We again calculate the $L^1$- and $L^\infty$-errors at time $T = 1$, using the cell averages of the computed and the exact solutions of (4.2). As in the one-dimensional case, the results, presented in Table 4.2, indicate the third-order convergence rate.

**Table 4.1.** Accuracy test for the linear advection problem (4.1), **T=1**

| N | $L^1$-error | rate | $L^\infty$-error | rate |
|---|---|---|---|---|
| 40 | 1.355e-03 | – | 3.384e-04 | – |
| 80 | 1.699e-04 | 3.00 | 4.245e-05 | 3.00 |
| 160 | 2.125e-05 | 3.00 | 5.313e-06 | 3.00 |
| 320 | 2.658e-06 | 3.00 | 6.645e-07 | 3.00 |
| 640 | 3.323e-07 | 3.00 | 8.307e-08 | 3.00 |
| 1280 | 4.154e-08 | 3.00 | 1.038e-08 | 3.00 |

**Table 4.2.** Accuracy test for the linear advection problem (4.2), **T=1**

| Grid | $L^1$-error | rate | $L^\infty$-error | rate |
|---|---|---|---|---|
| $16 \times 16$ | 1.206e-01 | – | 9.400e-02 | – |
| $32 \times 32$ | 1.623e-02 | 2.89 | 1.272e-02 | 2.89 |
| $64 \times 64$ | 2.056e-03 | 2.98 | 1.614e-03 | 2.98 |
| $128 \times 128$ | 2.577e-04 | 3.00 | 2.024e-04 | 3.00 |
| $256 \times 256$ | 3.224e-05 | 3.00 | 2.532e-05 | 3.00 |

### *4.2 One-dimensional problems*

*Example 3 – Burgers' equation.* In this example, we solve the IBVP for the one-dimensional Burgers' equation

$$\begin{cases} u_t + \left(\dfrac{u^2}{2}\right)_x = 0, \quad x \in [0, 2\pi], \\ \\ u(x,0) = 0.5 + \sin x, \end{cases} \tag{4.3}$$

with periodic boundary conditions. It is known that the unique entropy solution of (4.3) develops a shock discontinuity at time $t = 1$. In Fig. 4.1 we present the approximate solution at the post-shock time $T = 2$, computed by the scheme (2.9)–(2.11) with the reconstruction (3.4).

Notice, that even though the method provides a high resolution of the shock, one can observe the over- and undershootings near the discontinuity. This happens because the limiter $\theta_j^n$, defined in (3.3), is switched off (i.e., $\theta_j^n = 1$) at the local extrema.

It is possible to reduce these oscillations with the following recipe – we choose $\theta_j^n$ to be

$$\theta_j^n = \max\left\{ \min\left( 1 - \frac{|q_j^n(x_{j+\frac{1}{2}}) - \bar{u}_j^n|^{\alpha+3}}{(\Delta x)^\alpha}, \right.\right. \\ \left.\left. 1 - \frac{|q_j^n(x_{j-\frac{1}{2}}) - \bar{u}_j^n|^{\alpha+3}}{(\Delta x)^\alpha} \right), 0 \right\}, \quad \alpha \geq 1, \tag{4.4}$$

when $\bar{u}_j^n > \bar{u}_{j\pm1}^n$, or $\bar{u}_j^n < \bar{u}_{j\pm1}^n$. The modified reconstruction (3.4),(4.4) is still third-order in smooth regions, and at the same time, it reduces the oscillations near the discontinuities.

In general, any $\alpha \geq 1$ can be used in (4.4). Our numerical experiments have not indicated which value of $\alpha$ is optimal. Our experience shows that larger $\alpha$'s lead to smaller oscillations, but increase the numerical dissipation. In this example (see Fig. 4.2) and in the examples below, we have used $\alpha = 10$.

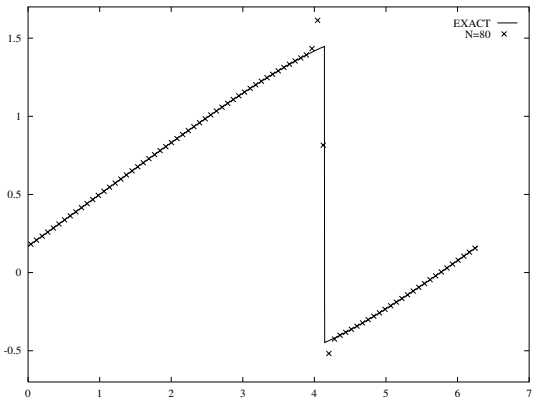


**Fig. 4.1.** Burgers equation (4.3); using reconstruction (3.4)

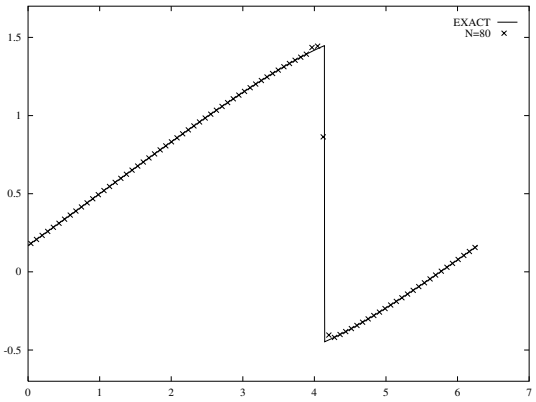


**Fig. 4.2.** Burgers equation (4.3); using reconstruction (3.4),(4.4)

*Example 4 – One-dimensional Euler equations of gas dynamics.* Here we consider the one-dimensional Euler system,

$$\frac{\partial}{\partial t}\begin{bmatrix}\rho\\ m\\ E\end{bmatrix}+\frac{\partial}{\partial x}\begin{bmatrix}m\\ \rho u^2+p\\ u(E+p)\end{bmatrix}=0,\qquad p=(\gamma-1)\cdot\Big(E-\frac{\rho}{2}u^2\Big), \tag{4.5}$$

where $\rho$, $u$, $m=\rho u$, $p$ and $E$ are the density, velocity, momentum, pressure and the total energy, respectively, and $\gamma=1.4$. We solve this system with the initial data

$$\mathbf{u}(x,0)=\begin{cases}\mathbf{u}_L=(1,0,2500)^{\mathrm{T}}, & 0\le x<0.1,\\ \mathbf{u}_M=(1,0,0.025)^{\mathrm{T}}, & 0.1\le x<0.9,\\ \mathbf{u}_R=(1,0,250)^{\mathrm{T}}, & 0.9\le x<1,\end{cases} \tag{4.6}$$

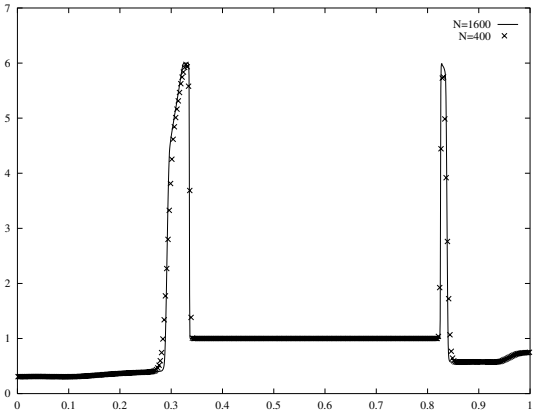


**Fig. 4.3.** Problem (4.5)–(4.6), density at **T=0.01**; using reconstruction (3.4)

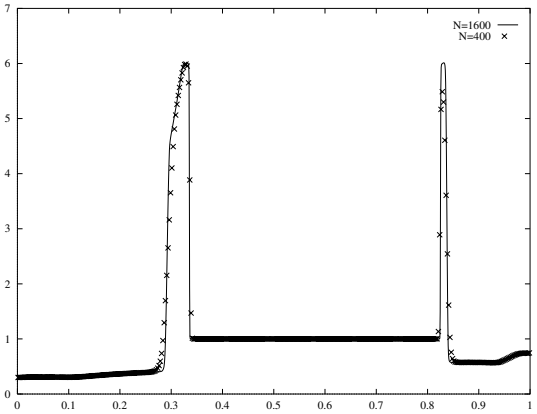


**Fig. 4.4.** Problem (4.5)–(4.6), density at **T=0.01**; using reconstruction (3.4), (4.4)

and solid boundary conditions, applied to both ends. The example describes the interaction of blast waves and was proposed by Woodward and Colella in [37].

To compute the approximate solution of (4.5)–(4.6), we use the scheme (2.9)–(2.11) with the reconstruction (3.4). The computations are done, using $N = 400$ grid points, and the solution is plotted together with a reference solution, obtained by the same method with $N = 1600$.

Figures 4.3, 4.5, and 4.7 show the density, the velocity, and the pressure at time $T = .01$. Notice, that if we use $400$ grid points, the second density spike has a height of $\sim 5.75$, which is better in comparison with the heights of $\sim 5.2$ obtained by the third-order staggered central scheme in [29], and $\sim 3.7$, obtained by the second-order Nessyahu-Tadmor scheme in [31]. This illustrates the higher resolution and smaller numerical dissipation of our method.

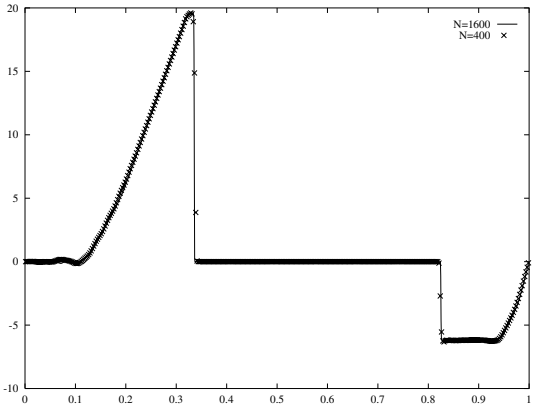


**Fig. 4.5.** Problem (4.5)–(4.6), velocity at **T=0.01**; using reconstruction (3.4)

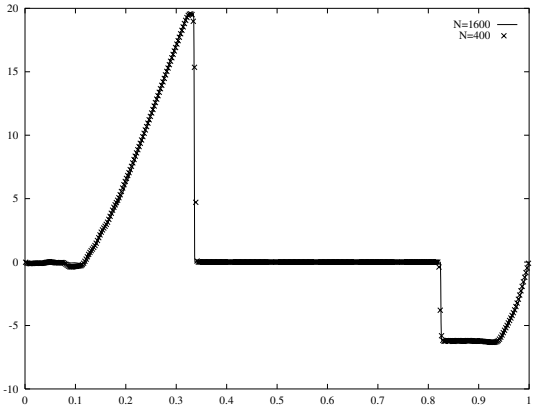


**Fig. 4.6.** Problem (4.5)–(4.6), velocity at **T=0.01**; using reconstruction (3.4), (4.4)

Figures 4.4, 4.6, and 4.8 show the solution of the same problem, computed again by the scheme (2.9)–(2.11), but this time coupled with the modified reconstruction (3.4),(4.4). The height of the second density spike here is $\sim 5.5$ which, as we have mentioned above, is due to the more dissipative nature of the modified reconstruction. The advantage of this approach is that it reduces the oscillations, as one can see on Figs. 4.15 and 4.16.

We also perform the computations at time $T = 0.03$. The results are presented in Figs. 4.9–4.16. We would like to point out that for $400$ grid points the maximum value of the density is $\sim 23$ (see Fig. 4.9), and it is $\sim 21$ (see Fig. 4.9), if we apply the limiter (4.4) at local extrema. Notice, that for the more dissipative third-order staggered central scheme in [29] this height is $\sim 20$.

Finally, we compute the solution of (4.5)–(4.6) at time $T = 0.038$, shown in Figs. 4.17–4.22. Here, the value of the second density spike is $\sim 5.5$ (see

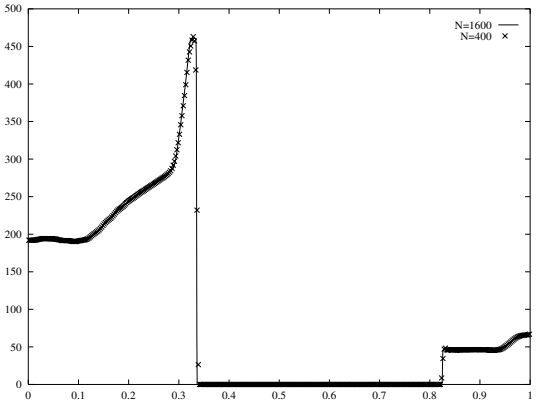


**Fig. 4.7.** Problem (4.5)–(4.6), pressure at **T=0.01**; using reconstruction (3.4)

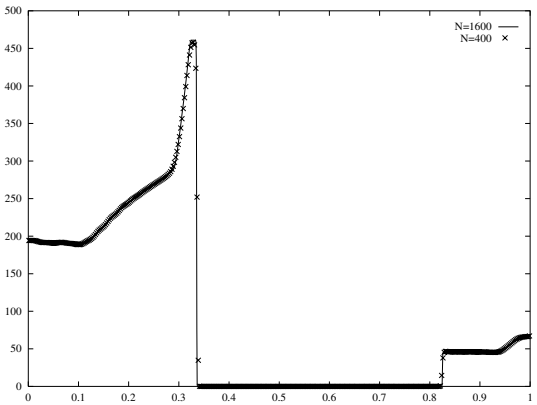


**Fig. 4.8.** Problem (4.5)–(4.6), pressure at **T=0.01**; using reconstruction (3.4), (4.4).

Fig. 4.17), and $\sim 5.2$, if we apply (4.4) (see Fig. 4.18). The corresponding number from [29] is $\sim 5$.

### *4.3 Two-dimensional problems*

*Example 5 – Two-dimensional convection-diffusion problem.* We consider the two-dimensional Burgers-type equation

$$u_t + (u^2)_x + (u^2)_y = \varepsilon(\nu(u)u_x)_x + \varepsilon(\nu(u)u_y)_y, \quad (x,y) \in [-1.5, 1.5] \times [-1.5, 1.5], \tag{4.7}$$

with a *strongly* degenerate diffusion coefficient

$$\nu(u) = \begin{cases} 0, & |u| \le 0.25, \\ 1, & |u| > 0.25. \end{cases}$$

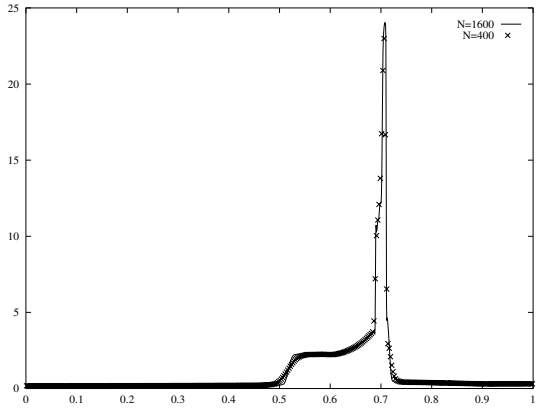


**Fig. 4.9.** Problem (4.5)–(4.6), density at **T=0.03**; using reconstruction (3.4)

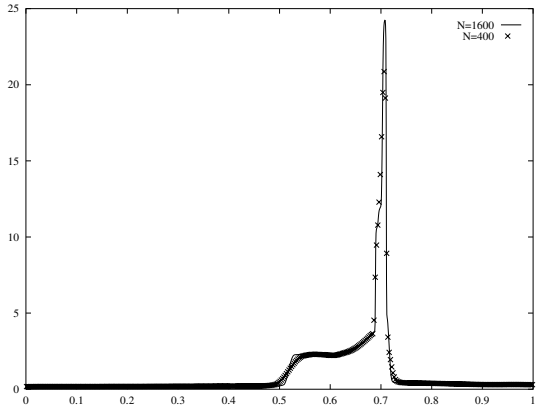


**Fig. 4.10.** Problem (4.5)–(4.6), density at **T=0.03**; using reconstruction (3.4), (4.4)

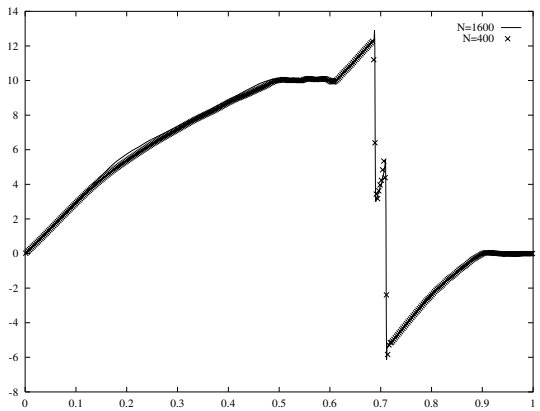


**Fig. 4.11.** Problem (4.5)–(4.6), velocity at **T=0.03**; using reconstruction (3.4)

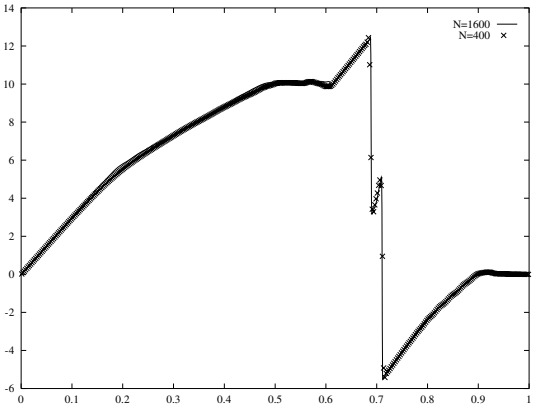


**Fig. 4.12.** Problem (4.5)–(4.6), velocity at **T=0.03**; using reconstruction (3.4), (4.4)

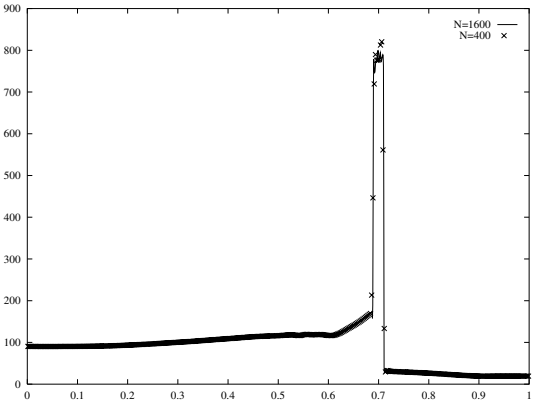


**Fig. 4.13.** Problem (4.5)–(4.6), pressure at **T=0.03**; using reconstruction (3.4)

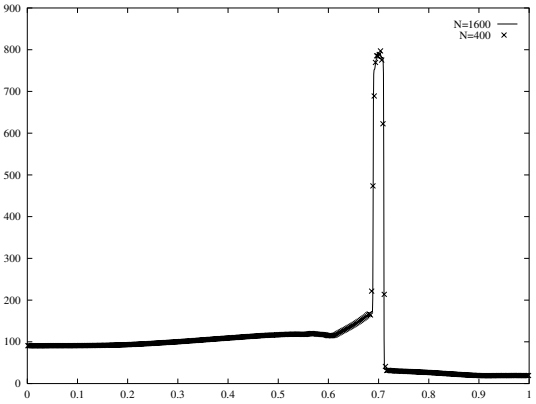


**Fig. 4.14.** Problem (4.5)–(4.6), pressure at **T=0.03**; using reconstruction (3.4), (4.4)

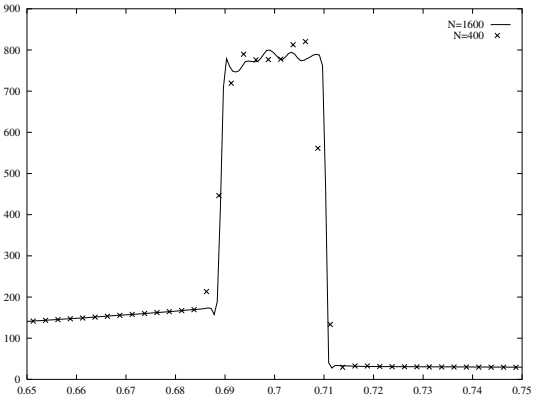


**Fig. 4.15.** Problem (4.5)–(4.6), pressure at **T=0.03**; using reconstruction (3.4); zoom at $[0.65, 0.75]$

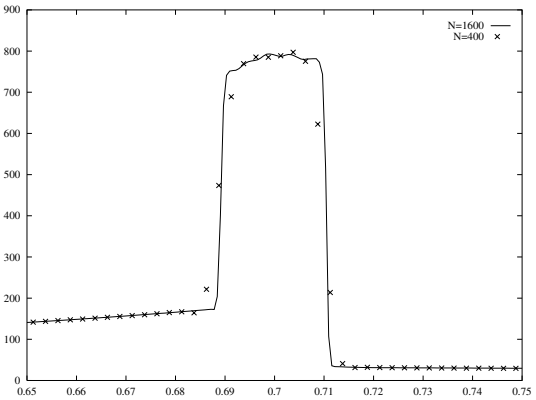


**Fig. 4.16.** Problem (4.5)–(4.6), pressure at **T=0.03**; using reconstruction (3.4), (4.4); zoom at $[0.65, 0.75]$

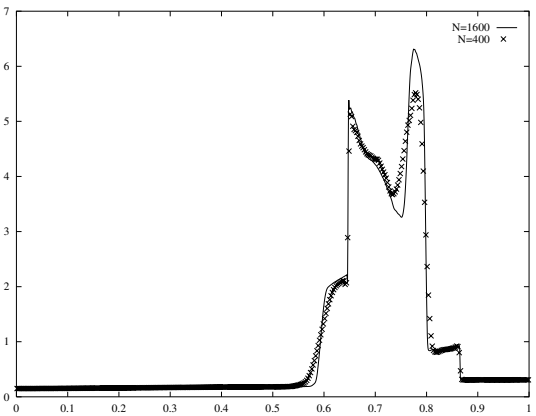


**Fig. 4.17.** Problem (4.5)–(4.6), density at **T=0.038**; using reconstruction (3.4)

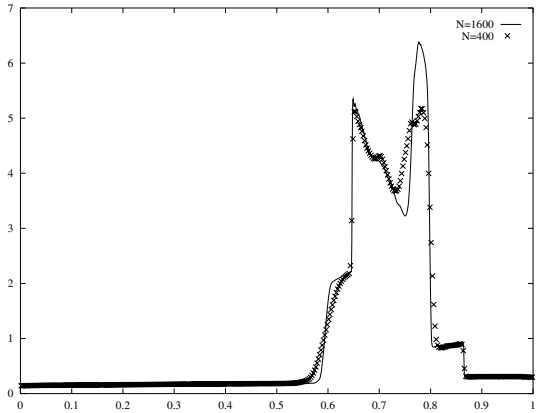


**Fig. 4.18.** Problem (4.5)–(4.6), density at **T=0.038**; using reconstruction (3.4), (4.4).

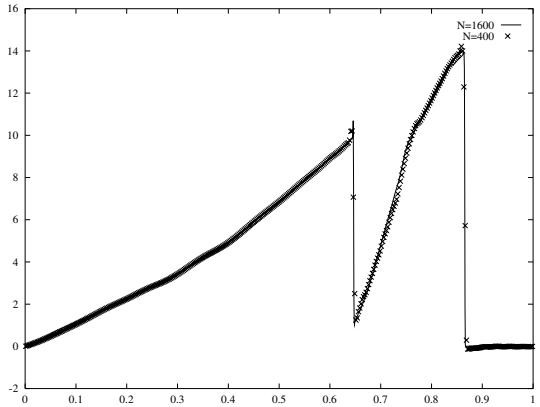


**Fig. 4.19.** Problem (4.5)–(4.6), velocity at **T=0.038**; using reconstruction (3.4)

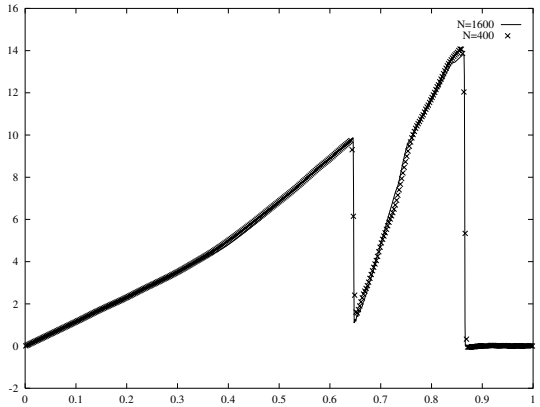


**Fig. 4.20.** Problem (4.5)–(4.6), velocity at **T=0.038**; using reconstruction (3.4), (4.4)

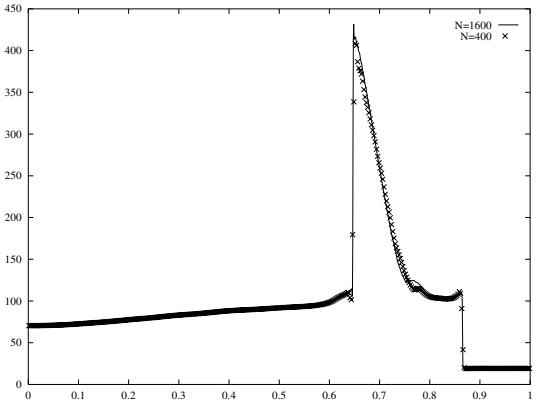


**Fig. 4.21.** Problem (4.5)–(4.6), pressure at **T=0.038**; using reconstruction (3.4)

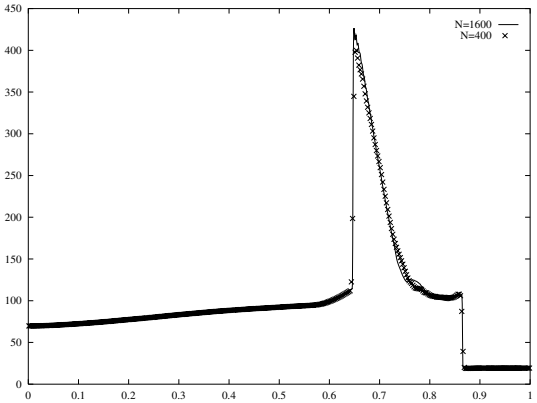


**Fig. 4.22.** Problem (4.5)–(4.6), pressure at **T=0.038**; using reconstruction (3.4), (4.4)

This equation is of hyperbolic nature when $u \in [-0.25, 0.25]$, and is parabolic elsewhere.

We solve (4.7), subject to the initial data

$$u(x,y,0) = \begin{cases} -1, & \text{if } (x-0.5)^2 + (y-0.5)^2 \le 0.16, \\ 1, & \text{if } (x+0.5)^2 + (y+0.5)^2 \le 0.16, \\ 0, & \text{otherwise.} \end{cases}$$

The numerical experiments are performed for $\varepsilon = 0.1$, and for $\varepsilon = 0$. In the first case we use the scheme (3.23), and in the second, pure hyperbolic case, we apply the scheme (3.20)–(3.22), coupled with the reconstruction (3.36)–(3.37).

Figures 4.23 and 4.24 show the computed solutions at time $T = 0.5$ in the hyperbolic and the hyperbolic-parabolic case, respectively. We would like to emphasize, that in both cases the resolution of the shock discontinuities is very high, and the transition between the hyperbolic and parabolic regions

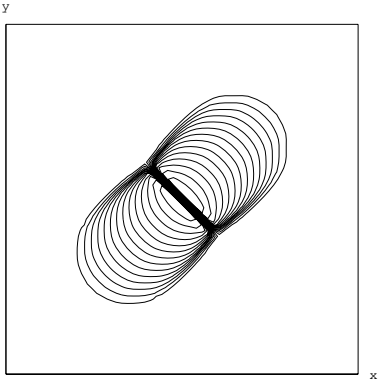


**Fig. 4.23.** Pure hyperbolic problem (4.7) with $\varepsilon = 0$, **T=0.5**; $60 \times 60$ grid

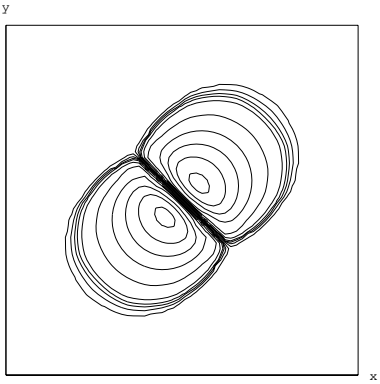


**Fig. 4.24.** Degenerate parabolic problem (4.7) with $\varepsilon = 0.1$, **T=0.5**; $60 \times 60$ grid

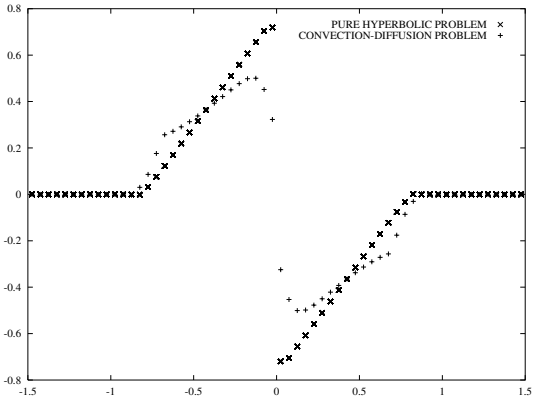


**Fig. 4.25.** Cross-section along the line $y = x$

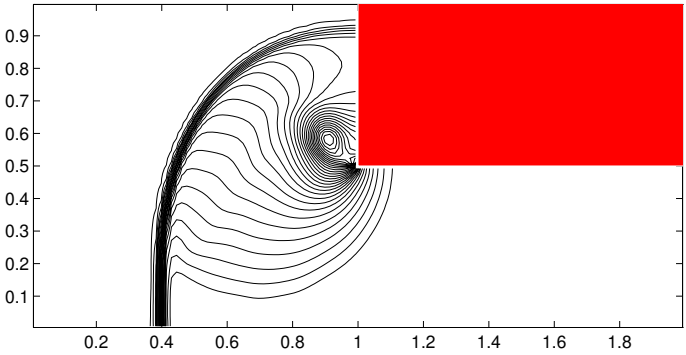


**Fig. 4.26.** Equation (4.8), density; **T=0.5**, $128 \times 64$ grid, 30 contours

is accurate. This can be clearly seen on the one-dimensional cross-section along the diagonal $y = x$ (see Fig. 4.25).

*Example 6 – Two-dimensional Euler equations of gas dynamics.* In this example, we consider the two-dimensional compressible Euler equations

$$\frac{\partial}{\partial t}\begin{bmatrix}\rho\\ \rho u\\ \rho v\\ E\end{bmatrix}+\frac{\partial}{\partial x}\begin{bmatrix}\rho u\\ \rho u^2+p\\ \rho uv\\ u(E+p)\end{bmatrix}+\frac{\partial}{\partial y}\begin{bmatrix}\rho v\\ \rho uv\\ \rho v^2+p\\ v(E+p)\end{bmatrix}=0,$$

$$p=(\gamma-1)\cdot\left[E-\frac{\rho}{2}(u^2+v^2)\right], \tag{4.8}$$

where $\rho$, $u$, $v$, $p$ and $E$ are the density, the $x$- and $y$-velocities, the pressure and the total energy, respectively. We solve (4.8) for an ideal gas ($\gamma = 1.4$) in the domain $[0,2]\times[0,0.5]\cup[0,1]\times[0.5,1]$, with the initial data corresponding to a vertical left-moving Mach 1.65 shock, positioned at $x = 1.375$. The initial shock propagates and then diffracts around a solid corner. We compute the solution at time $T = 0.5$, using the scheme (3.20)–(3.22) together with the reconstruction (3.36)–(3.37). Figures 4.26, 4.27, and 4.28 are contour plots of the density for $128\times64$, $256\times128$, and $512\times256$ grid points, respectively. The speed, $\sqrt{u^2+v^2}$, and the pressure, computed for $512\times256$ grid points, are shown in Figs. 4.29 and 4.30.

We would like to point out the remarkable resolution, achieved by our genuinely two-dimensional third-order central scheme, where none of the characteristic decomposition, dimensional splitting or evolution of nonconservative quantities is used.

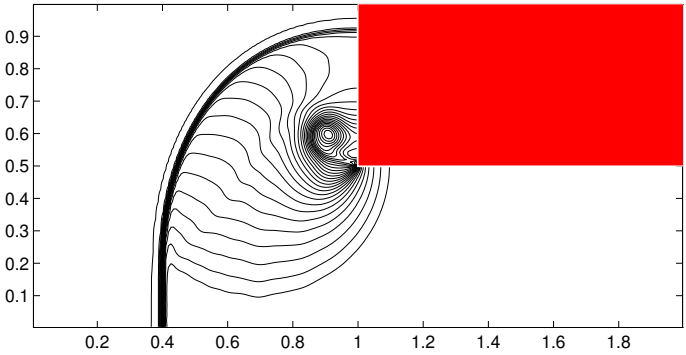


**Fig. 4.27.** Equation (4.8), density; **T=0.5**, $256 \times 128$ grid, 30 contours

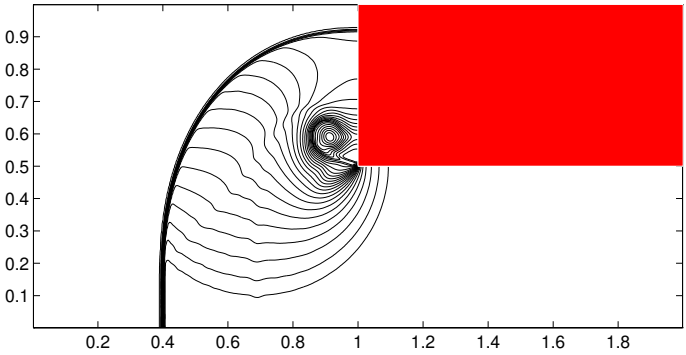


**Fig. 4.28.** Equation (4.8), density; **T=0.5**, $512 \times 256$ grid, 30 contours

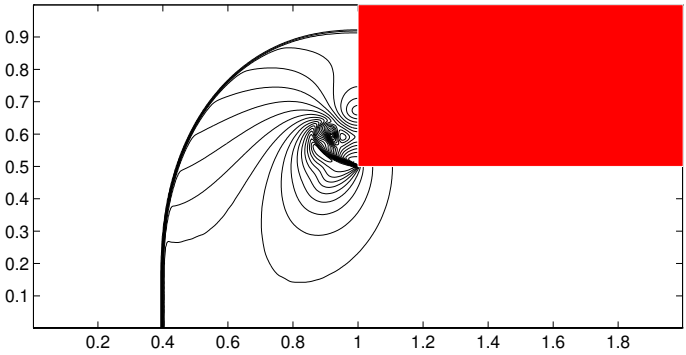


**Fig. 4.29.** Equation (4.8), speed; **T=0.5**, $512 \times 256$ grid, 20 contours

### *4.4 Two-dimensional incompressible Euler and Navier-Stokes equations*

In this example, we consider the two-dimensional equation

$$\omega_t + (u\omega)_x + (v\omega)_y = \nu\Delta\omega, \tag{4.9}$$

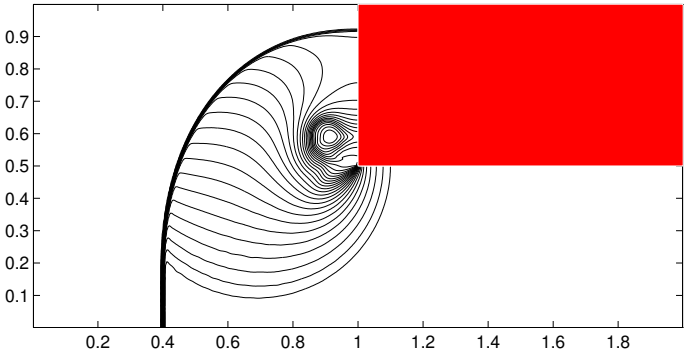


**Fig. 4.30.** Equation (4.8), pressure; **T=0.5**, $512 \times 256$ grid, 30 contours

where $\omega := v_x - u_y$ is the vorticity, and the velocity field $(u, v)$ is divergence-free, that is

$$u_x + v_y = 0. \tag{4.10}$$

The system (4.9)–(4.10) is a vorticity formulation of the incompressible Euler (for $\nu = 0$) or Navier-Stokes (for $\nu > 0$) equations. The equation (4.9) can be viewed as the two-dimensional conservation law

$$\omega_t + f(\omega)_x + g(\omega)_y = \nu \Delta\omega, \tag{4.11}$$

with a global flux $(f, g) := (u\omega, v\omega)$.

Our scheme (3.23), applied to (4.11), has the form

$$\begin{aligned} \frac{d}{dt}\bar{w}_{j,k}(t) = &-\frac{H^x_{j+\frac12,k}(t) - H^x_{j-\frac12,k}(t)}{\Delta x} \\ &-\frac{H^y_{j,k+\frac12}(t) - H^y_{j,k-\frac12}(t)}{\Delta y} + \nu Q_{j,k}(t), \end{aligned} \tag{4.12}$$

with the numerical convection fluxes

$$\begin{aligned} H^x_{j+\frac12,k} := &\left\{ u_{j+\frac12,k+\frac12}(\omega^{\mathrm{NW}}_{j+1,k} + \omega^{\mathrm{NE}}_{j,k}) + 4u_{j+\frac12,k}(\omega^{\mathrm{W}}_{j+1,k} + \omega^{\mathrm{E}}_{j,k}) \right. \\ &\left. + u_{j+\frac12,k-\frac12}(\omega^{\mathrm{SW}}_{j+1,k} + \omega^{\mathrm{SE}}_{j,k}) \right\} \Big/ \left\{ 12 \right\} - \frac{a^x_{j+\frac12,k}}{12} \\ &\times \left[ \omega^{\mathrm{NW}}_{j+1,k} - \omega^{\mathrm{NE}}_{j,k} + 4(\omega^{\mathrm{W}}_{j+1,k} - \omega^{\mathrm{E}}_{j,k}) + \omega^{\mathrm{SW}}_{j+1,k} - \omega^{\mathrm{SE}}_{j,k} \right], \end{aligned} \tag{4.13}$$

and

$$H^y_{j,k+\frac12} := \left\{ v_{j-\frac12,k+\frac12}(\omega^{\mathrm{SW}}_{j,k+1} + \omega^{\mathrm{NW}}_{j,k}) + 4v_{j,k+\frac12}(\omega^{\mathrm{S}}_{j,k+1} + \omega^{\mathrm{N}}_{j,k}) \right.$$

$$+v_{j+\frac{1}{2},k+\frac{1}{2}}(\omega^{\mathrm{SE}}_{j,k+1}+\omega^{\mathrm{NE}}_{j,k})\Bigg\}\Bigg/\Bigg\{12\Bigg\}-\frac{a^{y}_{j,k+\frac{1}{2}}}{12}$$

$$\times\Big[\omega^{\mathrm{SW}}_{j,k+1}-\omega^{\mathrm{NW}}_{j,k}+4(\omega^{\mathrm{S}}_{j,k+1}-\omega^{\mathrm{N}}_{j,k})+\omega^{\mathrm{SE}}_{j,k+1}-\omega^{\mathrm{NE}}_{j,k}\Big]. \tag{4.14}$$

The local speeds can be chosen, for example, as

$$a^{x}_{j+\frac{1}{2},k}:=|u_{j+\frac{1}{2},k}|,\qquad a^{y}_{j,k+\frac{1}{2}}:=|v_{j,k+\frac{1}{2}}|, \tag{4.15}$$

and the diffusion flux $Q_{j,k}$ can be approximated by the fourth-order central differencing,

$$Q_{j,k}=\frac{-\bar\omega_{j+2,k}+16\bar\omega_{j+1,k}-30\bar\omega_{j,k}+16\bar\omega_{j-1,k}-\bar\omega_{j-2,k}}{12(\Delta x)^2}$$

$$+\frac{-\bar\omega_{j,k+2}+16\bar\omega_{j,k+1}-30\bar\omega_{j,k}+16\bar\omega_{j,k-1}-\bar\omega_{j,k-2}}{12(\Delta y)^2}. \tag{4.16}$$

The intermediate values of the velocities, which appear in (4.13) and (4.14), are computed by the fourth-order formula

$$u_{j+\frac{1}{2},k}=\frac{-u_{j+2,k}+9u_{j+1,k}+9u_{j,k}-u_{j-1,k}}{16},$$

$$v_{j,k+\frac{1}{2}}=\frac{-v_{j,k+2}+9v_{j,k+1}+9v_{j,k}-v_{j,k-1}}{16}. \tag{4.17}$$

To perform these computations, we need to recover the values of the velocities at the grid points $\{u_{j,k},v_{j,k}\}$ from the known vorticity $\{\omega_{j,k}\}$ at every time step. There are a lot of methods of the velocity recovery (see, e.g., [24] and the references therein). In this example, we use the stream-function $\psi$, where $u=\psi_y$, $v=-\psi_x$, and $\psi$ is a solution of the Poisson equation $\Delta\psi=-\omega$. We solve the nine-points Laplacian $\Delta\psi_{j,k}=-\omega_{j,k}$, and we substitute the computed values of the stream-function in

$$u_{j,k}=\frac{-\psi_{j,k+2}+8\psi_{j,k+1}-8\psi_{j,k-1}+\psi_{j,k-2}}{12\Delta y},$$

$$v_{j,k}=\frac{\psi_{j+2,k}-8\psi_{j+1,k}+8\psi_{j-1,k}-\psi_{j-2,k}}{12\Delta x}. \tag{4.18}$$

We now apply our scheme (4.12)–(4.18), coupled with the reconstruction (3.36)–(3.37), to the Navier-Stokes equation (4.9)–(4.10)) with $\nu=0.05$, subject to the smooth periodic initial data (taken from [5]),

$$u(x,y,0)=-\cos x\sin y,\qquad v(x,y,0)=\sin x\cos y, \tag{4.19}$$

The exact solution to this problem is given by

$$u(x,y,t)=-\mathrm{e}^{-2\nu t}\cos x\sin y,\qquad v(x,y,t)=\mathrm{e}^{-2\nu t}\sin x\cos y.$$

**Table 4.3.** Accuracy test for the Navier-Stokes equation (4.9)–(4.10),(4.19), $\nu = 0.05$; errors at $T = 2$

| $Nx \times Ny$ | $L^\infty$-error | rate | $L^1$-error | rate | $L^2$-error | rate |
|---|---|---|---|---|---|---|
| $32 \times 32$ | 2.104e-03 | – | 2.762e-02 | – | 5.625e-03 | – |
| $64 \times 64$ | 2.788e-04 | 2.92 | 3.653e-03 | 2.92 | 7.404e-04 | 2.93 |
| $128 \times 128$ | 3.556e-05 | 2.97 | 4.634e-04 | 2.98 | 9.391e-05 | 2.98 |
| $256 \times 256$ | 4.444e-06 | 3.00 | 5.811e-05 | 3.00 | 1.176e-05 | 3.00 |

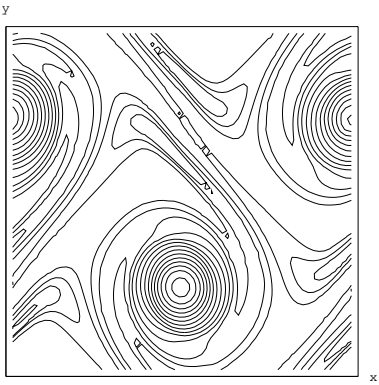


**Fig. 4.31.** Incompressible Euler equation (4.9)–(4.10),(4.20); **T=10**, $64 \times 64$ grid

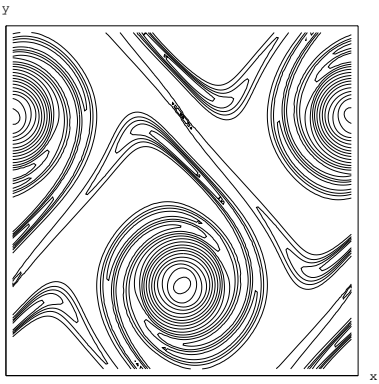


**Fig. 4.32.** Incompressible Euler equation (4.9)–(4.10),(4.20); **T=10**, $128 \times 128$ grid

The purpose of this numerical experiment is to check the accuracy of our scheme. The approximate solution is computed at time $T = 2$, and the errors for the vorticity are measured in the $L^\infty$-, $L^1$- and $L^2$-norms. The results are presented in Table 4.3. We would like to point out that due to the genuinely multidimensional nature of our scheme, the convergence rate is higher than the convergence rate reported in [16], where the 'dimension-by-dimension' approach was used.

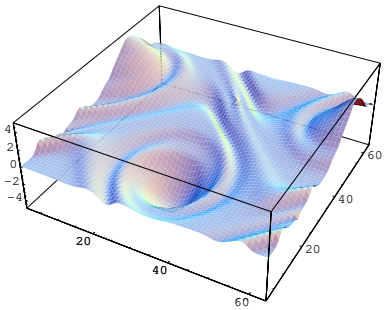


**Fig. 4.33.** Incompressible Euler equation (4.9)–(4.10),(4.20); **T=10**, $64 \times 64$ grid

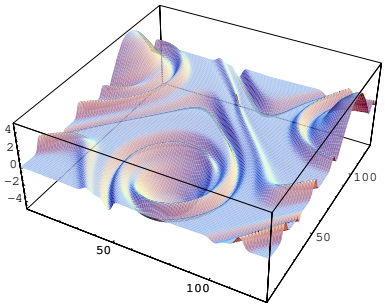


**Fig. 4.34.** Incompressible Euler equation (4.9)–(4.10),(4.20); **T=10**, $128 \times 128$ grid

Next, the scheme (4.12)–(4.18) together with the reconstruction (3.36)–(3.37) is implemented for the periodic double shear-layer model problem (taken from [3]). We solve the Euler equation, (4.9)–(4.10) with $\nu = 0$, subject to the $(2\pi, 2\pi)$-periodic initial data,

$$(4.20)\quad u(x,y,0) = \begin{cases} \tanh(\frac{1}{\rho}(y-\pi/2)), & y \le \pi, \\ \tanh(\frac{1}{\rho}(3\pi/2-y)), & y > \pi, \end{cases} \qquad v(x,y,0) = \delta \cdot \sin x.$$

We use the value $\pi/15$ for the "thick" shear-layer width parameter $\rho$, and the value $0.05$ for the perturbation parameter $\delta$. Figures 4.31 and 4.32 are the contour plots of the solution at time $T = 10$ with $64 \times 64$ and $128 \times 128$ grid points, respectively. The three-dimensional plots of the same results are shown in Figs. 4.33 and 4.34. The performed numerical experiments demonstrate that our scheme provides sharper resolution than the third-order 'dimension-by-dimension' central scheme in [16]. This is due to the genuinely multidimensional nature of our method.

*Acknowledgements.* The authors would like to thank Prof. S. Karni and Dr. S. Noelle for the fruitful discussions and helpful comments. The work of A. Kurganov was supported in part by the NSF Group Infrastructure Grant and the NSF Grant DMS-0073631.

## References


1. A. M. Anile, V. Romano, G. Russo, Extended hydrodynamical model of carrier transport in semiconductors. SIAM J. Appl. Math. (Preprint)
2. P. Arminjon, M.-C. Viallon, Généralisation du schéma de Nessyahu-Tadmor pour une équation hyperbolique à deux dimensions d'espace. C.R. Acad. Sci. Paris, t. 320, série I (1995), pp. 85–88
3. J.B. Bell, P. Colella, H.M. Glaz, A second-order projection method for the incompressible Navier-Stokes equations. J. of Comp. Phys. **85**, 257–283 (1989)
4. F. Bianco, G. Puppo, G. Russo, High order central schemes for hyperbolic systems of conservation laws. SIAM J. Sci. Comp. (to appear)
5. A. Chorin, Numerical solution of the Navier-Stokes equations. Math. Comp. **22**, 745–762 (1968)
6. B. Engquist, O. Runborg, Multi-phase computations in geometrical optics. J. Comp. Appl. Math. **74**, 175–192 (1996)
7. K.O. Friedrichs, Symmetric hyperbolic linear differential equations. Comm. Pure Appl. Math. **7**, 345–392 (1954)
8. A. Harten, High resolution schemes for hyperbolic conservation laws. J. of Comp. Phys. **49**, 357–393 (1983)
9. A. Harten, B. Engquist, S. Osher, S.R. Chakravarthy, Uniformly high order accurate essentially non-oscillatory schemes III. J. of Comp. Phys. **71** 231–303 (1987)
10. G.-S. Jiang, C.-W. Shu, Efficient implementation of weighted ENO schemes. J. of Comp. Phys. **126**, 202–228 (1996)
11. G.-S. Jiang, E. Tadmor, Non-oscillatory central schemes for multidimensional hyperbolic conservation laws. SIAM J. Sci. Comp. **19**, 1892–1917 (1998)
12. R. Kupferman, Simulation of viscoelastic fluids; Couette-Taylor flow. J. of Comp. Phys. (to appear)
13. R. Kupferman, A numerical study of the axisymmetric Couette-Taylor problem using a fast high-resolution second-order central scheme. SIAM J. Sci. Comp. **20**, 858–877 (1998)
14. R. Kupferman, E. Tadmor, A fast high-resolution second-order central scheme for incompressible flows. Proceedings of the National Academy of Sciences **94**, 4848–4852 (1997)
15. A. Kurganov, Conservation laws: stability of numerical approximations and nonlinear regularization. Ph.D. Thesis, Tel-Aviv University, Israel (1997)
16. A. Kurganov, D. Levy, A third-order semi-discrete central scheme for conservation laws and convection-diffusion equations. SIAM J. Sci. Comp (to appear)
17. A. Kurganov, E. Tadmor, New high-resolution central schemes for nonlinear conservation laws and convection-diffusion equations. J. of Comp. Phys. **160**, 241–282 (2000)
18. A. Kurganov, E. Tadmor, New high-resolution semi-discrete schemes for Hamilton-Jacobi equations. J. of Comp. Phys. **160**, 720–742 (2000)
19. P.D. Lax, Weak solutions of nonlinear hyperbolic equations and their numerical computation. Comm. Pure Appl. Math. **7**, 159–193 (1954)
20. B. van Leer, Towards the ultimate conservative difference scheme, V. A second order sequel to Godunov's method. J. of Comp. Phys. **32**, 101–136 (1979)
21. D. Levy, G. Puppo, G. Russo, Central WENO schemes for hyperbolic systems of conservation laws. Math. Model. and Numer. Anal. **33**:3, 547–571 (1999)
22. D. Levy, G. Puppo, G. Russo, A third order central WENO scheme for 2D conservation laws. Appl. Numer. Math. (to appear)

23. D. Levy, G. Puppo, G. Russo, Compact central WENO schemes for multidimensional conservation laws. (submitted)
24. D. Levy, E. Tadmor, Non-oscillatory central schemes for the incompressible 2-D Euler equations. Math. Res. Lett. **4**, 1–20 (1997)
25. C.-T. Lin, E. Tadmor, $L^1$-stability and error estimates for approximate Hamilton-Jacobi solutions. Numerische Mathematik
26. C.-T. Lin, E. Tadmor, High-resolution non-oscillatory central schemes for Hamilton-Jacobi Equations. SIAM J. Sci. Comp. (to appear)
27. X.-D. Liu, S. Osher, Nonoscillatory high order accurate self similar maximum principle satisfying shock capturing schemes. I. SIAM J. Numer. Anal. **33**, 760–779 (1996)
28. X.-D. Liu, S. Osher, T. Chan, Weighted essentially non-oscillatory schemes. J. of Comp. Phys. **115**, 200–212 (1994)
29. X.-D. Liu, E. Tadmor, Third order nonoscillatory central scheme for hyperbolic conservation laws. Numerische Mathematik **79**, 397–425 (1998)
30. A.A. Medovikov, High order explicit methods for parabolic equations. BIT **38**:2, 372–390 (1998)
31. H. Nessyahu, E. Tadmor, Non-oscillatory central differencing for hyperbolic conservation laws. J. Comp. Phys. **87**, 408–463 (1990)
32. S. Osher, E. Tadmor, On the convergence of difference approximations to scalar conservation laws. Math. Comp. **50** 19–51 (1988)
33. V. Romano, G. Russo, Numerical solution for hydrodynamical models of semiconductors. $M^3$AN (Preprint)
34. C.-W. Shu, Total-variation-diminishing time discretizations. SIAM J. Sci. Comp. **6**, 1073–1084 (1988)
35. C.-W. Shu, Numerical experiments on the accuracy of ENO and modified ENO schemes. J. Sci. Comp. **5**:2, 127–149 (1990)
36. C.-W. Shu, S. Osher, Efficient implementation of essentially non-oscillatory shock-capturing schemes. J. Comp. Phys. **77**, 439–471 (1988)
37. P. Woodward, P. Colella, The numerical solution of two-dimensional fluid flow with strong shocks. J. Comp. Phys. **54**, 115–173 (1988)